RUGA MECHANICS OF COMPOSITE MEDIA WITH SOFT INCLUSIONS

BY

MOHAMED EZZELDIN ELSAYED AHMED ABDELMEGUID

THESIS

Submitted in partial fulfillment of the requirements
for the degree of Master of Science in Civil Engineering
in the Graduate College of the
University of Illinois at Urbana-Champaign, 2017

Urbana, Illinois

Adviser:

Assistant Professor Ahmed Elbanna

ABSTRACT

This thesis presents an investigation for the elastic deformation of two-phase fibril composites with soft inclusions, specifically, the influence of soft inclusions on the behavior of fibrils under compressive loading. It is demonstrated that the inclusion of soft material in the fibril matrix substantially alters the post-bifurcation response of elastic fibrils. First, nonlinear finite element analysis is used to demonstrate that due to localized instabilities, fibrils with soft inclusions exhibit negative post-buckling stiffness. The local instability is postulated to follow the same post-buckling behavior as a beam on an elastic foundation, through a semi-analytical approach, it is shown that an unstable post-bifurcation response emerges. Additionally, using numerical analysis, careful patterning of the inclusions is shown to induce complex surface topography attributed to the local buckling modes, such as wrinkles and folds. Furthermore, through natural frequency eigenvalue analysis, it is demonstrated that fibrils with soft inclusions in the post-buckling region have local modes with negative ω^2. Negative ω^2 is only observed in negative stiffness systems and associated with local modes of instability. Through Bloch wave analysis it is observed that due to the complex deformation modes of buckled fibrils with soft inclusions, widening band-gaps that are proportional to the prescribed load emerge. The findings presented in this thesis provide alternatives to the manufacturing of negative stiffness systems that relies on curved beam elements. It also serves to introduce the possibility of utilizing soft inclusions in achieving controllable surface morphologies. Finally, demonstrate the possibility of modulating acoustic bandgaps and optimizing damping properties of composites through end-shortening.

To my mother

ACKNOWLEDGEMENTS

I would like to express my sincere gratitude to my advisor Professor Ahmed E. Elbanna for his guidance and support throughout this research endeavor. Professor Elbanna has been a great mentor and an amazing source of inspiration. His vast pool of knowledge and understanding have helped me overcome the many difficulties I faced during my M.S. studies and research.

Thank you to all the members of the Mechanics of Complex Systems Laboratory for all the help and advice. In particular, thank you to Qianli Chen for helping me with the technical difficulties and providing me with all the necessary resources to produce this manuscript. Also, thank you to Ahmed Ghareeb for our insightful discussions.

I would like to thank my mother Hanaa Elhabrouk, for all the love, sacrifices, sleepless nights, and support throughout my life. My dad Ezzeldin Nasr for his advice and for instilling in me all his work ethics and dedication. I would like to thank my brother Sherif for providing me a great example to follow.

Finally, I would like to thank my wife Heba Kamel for all the love and support. Heba has always been there for me through thick and thin; her faith in me was a continuous source of motivation that kept me going and pushed me forward.

TABLE OF CONTENTS

CHAPTER 1

INTRODUCTION

1.1 Background and Motivation

Understanding the mechanics of composite materials is a long-standing quest in science and engineering. With the emergence of new manufacturing technologies, such as 3D printing [1] and fabrication using pop ups, folding, and bending [2, 3, 4], it has become possible to realize material systems with non-classical properties, including origami structures, meta-beams, and functionally-graded materials. These materials exhibit tunable response as a direct consequence of a structured micro-mechanical building block that is arranged in a manner which dictates the overall material performance. Examples include tunable compressive modulus [5], tunable surface morphology and band gap response [6, 7, 8].

The main focus in the literature thus far has been primarily on the behavior of soft matrix reinforced with stiffer inclusions [2, 9], or on the response of porous media [10, 11, 12], aiming to enhance the material properties. Recently there has been some interest in analyzing mechanics of composites with soft inclusions in a stiffer matrix. For example, Style et al. [13] demonstrated that it is possible to enhance the stiffness of solids by using liquid inclusions through leveraging surface tension effects. Several other studies discussed the influence of adding softer phase-changing materials to concrete to enhance its thermal characteristics [14, 15]. The mechanical response of composites with softer inclusions continues to be largely un-explored.

Another emerging theme in applied mechanics that is currently under study is ruga-mechanics [16], which is concerned with corrugation patterns, such as wrinkles, creases, and folds that emerge on solid surfaces. These surface topographies are found ubiquitously in nature, perhaps the most common example is the human brain [17]. These instabilities and surface pattern transformations have been mainly

analyzed in two-layer material systems in which a thin stiff layer is laid upon a softer substrate [18]. A direct extension of this, and possibly with more complex response, may be thought of as a stiff matrix with softer inclusions such that in the vicinity of the inclusions, the system behaves locally as a two-layer material system. This paper explores the rich mechanics of these composite systems.

Although instabilities have classically been linked with structural failure, numerous analytical [19, 20], computational [21, 22], and experimental [23, 24, 25] studies in the recent years suggest that such instabilities may be harnessed to trigger changes in acoustic, optical, and mechanical properties of materials [26, 27]; opening new pathways for the realization of programmable matter [28]. For example, Singamaneni et al. [29] demonstrated that tunnability of photonic properties is possible in periodic porous structures through the control of mechanical instabilities at the sub-micron scale. Coulais et al. [30] has shown that meta-beams may be designed through patterning of voids to exhibit negative post-buckling stiffness, which may be utilized to produce extreme damping under dynamic load. Timothy Klatt [31] presented an analytical and numerical scheme demonstrating that through controlled buckling of small-scale constituents it is possible to achieve negative overall stiffness, which leads to superior damping characteristics. While local buckling of stiff fibers in softer matrix [32], or local buckling of ribs in a porous structure, has been widely investigated, there is a gap in the literature when it comes to local buckling phenomena in composites with softer inclusions. Intuitively, if the inclusion is soft enough compared to the matrix, it will not suppress the buckling of the matrix ribs. However, unlike the case of porous materials, the soft inclusions provide non-zero resistance to the buckling of the ribs, which may trigger higher order buckling mode and lead to a richer static and dynamic post-buckling response [33].

This thesis aims to fill the literature gap regarding the mechanics of composites with soft inclusions under overall compressive loading and demonstrates unexpected outcomes particular to the soft inclusion case that are not realizable in the limit of zero stiffness inclusion. It demonstrates using analytical and numerical models the possibility of achieving negative post-buckling stiffness even if just a single soft inclusion is used. Furthermore, it illustrates the rich surface morphology that is facilitated by patterning these soft inclusions.

The thesis also presents a study of the dynamic response of fibrils with soft inclusions demonstrating that buckled fibrils which exhibit discontinuous buckling have

localized modes with negative frequency w^2 indicating the unstable post-buckling response associated with local instabilities. Furthermore, through its rich and complex deformations patterns fibril with soft inclusions can yield a band gap structure that can be tuned and utilized in the applications of vibration isolation and wave guiding.

1.2 Thesis Overview

This thesis presents a detailed study of the behavior of fibrils with soft inclusions in its post-buckling configuration.

- *Chapter 2*, introduces one of the principles of this thesis, which is that fibrils with soft inclusions can produce discontinuous buckling. The aim of this chapter is to demonstrate the role of the soft inclusion in creating a different bifurcation path that results in an unstable post-buckling response. We further introduce the formation of wrinkles on the surface of the fibril due to the matrix material buckling over a softer substrate, resembling thin films buckling on elastic substrate.

- *Chapter 3*, outlines the methodology used to evaluate the response of a composite with stiff matrix and soft inclusions. The governing balance equations and the constitutive model of the hyperelastic constituents is introduced. In addition, the framework for studying the dispersion relation for waves propagating in an elastic media is provided.

- *Chapter 4*, demonstrates the post-buckling response of the fibril with a soft inclusion using nonlinear variational analysis for a beam resting on an elastic foundation. In order to demonstrate the local unstable response, a semi-analytical approach for this problem is presented. Furthermore, the impact of the foundation (substrate) stiffness is studied.

- *Chapter 5*, presents the results of finite element simulations to demonstrate that fibrils with soft inclusions exhibit negative post-buckling response. These results complement and validate the results obtained in Chapter 4. In addition, an investigation of the impact of the inclusion dimensions and material

properties is conducted, illustrating the impact of inclusions in the overall behavior of the composite fibril. This study is then expanded to demonstrate the different deformation modes attainable for varying geometry, arrays, and layered stiffness.

- *Chapter 6*, presents the dynamic analysis results. Natural frequency extraction is conducted for the beam to understand the role of the negative post-buckling stiffness and identify the transition of local modes to negative w^2. Furthermore, through Bloch wave analysis, we demonstrate the emergence and evolution of band gaps in fibrils with soft inclusions.

- *Chapter 7*, summarize and conclude the thesis. The findings in Chapter 4, 5, and 6 are discussed along with their implications on the design of composites with controllable properties.

CHAPTER 2

A GLIMPSE IN POST-BUCKLING RESPONSE

2.1 Discontinuous Buckling

Buckling of straight beams under axial compressive load is one of the most fundamental problems in structural engineering, and is indeed considered as the most basic example of elastic instability. Elastic instability has been studied rigorously for all different type of structures. However, the starting point for these analyses was Euler elastica[34], which gave approximate estimate for the buckling load and post-buckling behavior appropriate for slender beams. Timoshinko[35] further expanded on the work of Euler and proposed to incorporate shear effects into the beam theory, which improved the estimates provided in Euler elastica for wider beams. We note that the solution of the Euler elastica for a straight beam results in a positive post-buckling stiffness of the beam. Nonlinear finite element analysis of the same problem yields similar results. Under sufficient axial compression, homogeneous fibrils with aspect ratio of 10% experience global mechanical instability and buckle. Consequently, the fibril ability to support load is substantially reduced, yet the post-buckling stiffness remains positive as shown in Fig.2.1a .

While this is the case for slender straight beams, it was demonstrated that for wider beams, meta-beams [30], or sufficiently curved beams [36], the post-buckling stiffness becomes negative. This response is referred to as discontinuous buckling. One of the main objectives of this thesis is to demonstrate that a straight beam with soft inclusions can also exhibit discontinuous buckling as shown in Fig.2.1a. In the presence of the soft inclusion, the global mechanical instability is followed by a local instability that results in the fibril following an unstable bifurcation path with a post-buckling negative stiffness response as shown in Fig.2.1c.

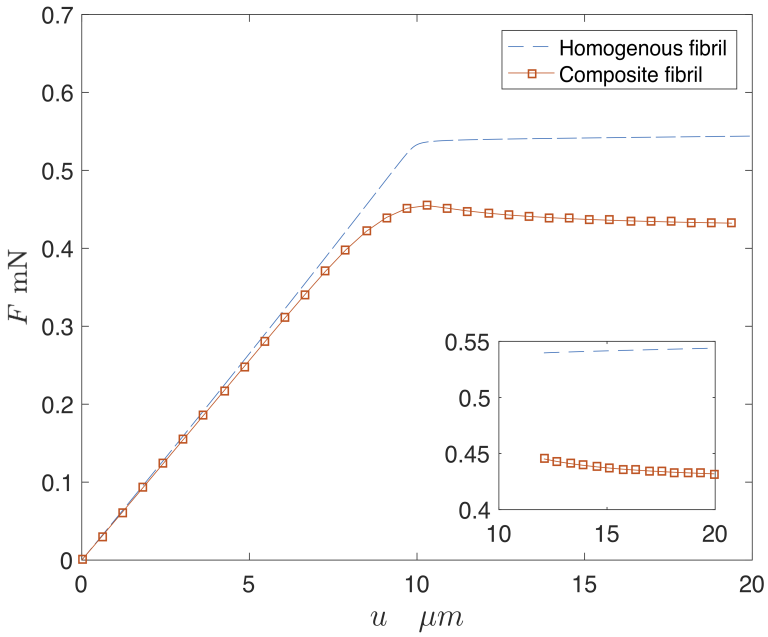

(a)

(b) (c)

Figure 2.1: (a) The reaction force vs end shortening diagram and the buckled shapes, illustrating the different post buckling behavior of (b) homogeneous fibril which undergoes traditional stable post-buckling behavior with a positive post-buckling slope,and (c) composite fibril with embedded inclusions that exhibit unstable post-buckling behavior with observable negative slope.

2.2 Wrinkles

Another interesting feature associated with the behavior of fibrils with soft inclusions is the emergence of wrinkles on the surface of the fibril due to local buckling. Wrinkling is found ubiquitously in nature, such as human brains or skin wrinkles. The term wrinkling is attributed to the buckling of stiff thin layer of film over a soft substrate underneath. Human skin for example is made up of 3 layers, with the top-most layer being the stiffest; aging results in the formation of compressive

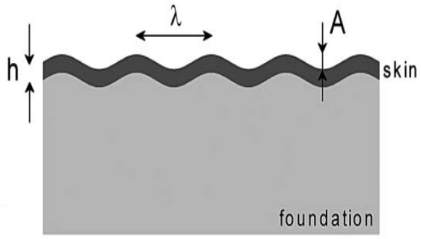

Figure 2.2: The wrinkling of skin due to buckling of a thin stiff layer of a softer foundation, where h is the thickness of the thin film layer, A is the amplitude of buckling, and λ is the wave length[37].

stresses that causes skin to wrinkle as shown in Fig.2.2 [37]. Generally, the reason behind the buckling of the thin film could be compressive load, thermal loads, or swelling.

To further understand this phenomenon, let's first consider the problem of a plate that is under axial compression. Energy minimization dictates that it is more favorable for the plate to buckle than compress. The buckling of plates is governed by Eqn. 2.1; under sufficient compressive load the plate buckles and the deformation pattern is described by a half sine mode.

$$D\nabla^4 w + \hat{N}_{\alpha\beta} w_{,\alpha\beta} = 0 \tag{2.1}$$

If the plate is resting on an elastic substrate, the deformation of the thin film causes the energy of the substrate to also increase. While initially the half sine mode was most favorable for the plate, bonding the plate to a soft substrate changes that. The half sine deformation pattern would cause a significant increase in the state of energy for the overall system. Accordingly, the plate buckling follows higher favorable deformation modes that minimize the overall energy [38]. A common approach to model the plate buckling is using idealizing the substrate as a Winkler foundation consisting of elastic springs [39]. This model approximates the buckling mode for compressible substrate through Eqn.2.2 [40].

$$\lambda = 2\pi h \left[\frac{H\hat{E}_p(1-2\nu_s)}{12h\hat{E}_s(1-\nu_s)^2} \right]^{\frac{1}{4}} \tag{2.2}$$

Where h is the plate thickness, H is the thickness of the substrate. $\hat{E} = E/(1-\nu^2)$ such that E is the Young's modulus, ν is the Poisson's ratio, and subscripts p and s indicates plate and substrate, respectively. For incompressible material with $\nu = 0.5$, this model breaks down and the determination of the foundation contribution is more complex.

The role of distributing soft inclusions within a stiff matrix composite acts in a similar manner, where every section can be treated as film over an elastic substrate. As compressive load is applied, the stiff matrix in the vicinity of the inclusion wants to buckle; however, since the stiff matrix is resting on a soft substrate, the buckling mode is dependent on the properties of the layers under the stiff matrix. Although, after the fibril buckles globally, different sections are under different types of loading. This allows for changes in the local buckling modes based on its location within the fibril. In some cases, local buckling can occur prior to global buckling depending on the slenderness ratio of the fibril compared to the stiff rib that is resting over the elastic substrate.

In this thesis, a similar model is proposed, where the local buckling behavior is modelled as a beam resting on an elastic foundation, for thin plates this assumption is quite valid. Due to the complexity of computing the foundation elastic modulus, a numerical finite element model is used to obtain an approximate value. This analysis is limited to the behavior of the inclusion located at mid-span of the fibril, and undergoing symmetric loading conditions in the post buckling configuration.

CHAPTER 3

METHODOLOGY

3.1 Governing Equations

Let us consider the one-to-one mapping denoting the motion to be

$$\mathbf{x} = \chi(\mathbf{X}, t) \tag{3.1}$$

Accordingly, the deformation gradient becomes

$$\mathbf{F} = \frac{\partial \mathbf{x}}{\partial \mathbf{X}} \tag{3.2}$$

For initial domain $\Omega_o \subset \mathbb{R}$ and current domain $\Omega(t)$, an applied traction $\mathbf{t}$ and in the absence of body forces, the balance of linear momentum is reduced to

$$\frac{d}{dt}\int_{\Omega(t)} \rho(\mathbf{x}, t)\mathbf{v}(\mathbf{x}, t)dx = \int_{\partial\Omega(t)} \mathbf{t}(\mathbf{x}, t)dx \tag{3.3}$$

Through conservation of mass and Cauchy theorem, the above equation can be reduced to the following form

$$\int_{\Omega(t)} \rho(\mathbf{x}, t)\dot{\mathbf{v}}(\mathbf{x}, t)dx = \int_{\partial\Omega(t)} \mathbf{T}.\mathbf{n} \quad dx \tag{3.4}$$

where $\mathbf{T}$ is Cauchy stress tensor. Implementing the divergence theorem, the final form of the balance of linear momentum in its Eulerian perspective is given as:

$$T_{ij,j} = \rho\dot{v}_i \tag{3.5}$$

It is convenient to work in the undeformed perspective as the information known is given in the underformed configuration, thus transforming into the Lagrangian perspective to obtain

$$S_{ij,j} = \rho_o \dot{V}_i = \rho_o \ddot{\chi}_i \tag{3.6}$$

where S_{ij} is the first order Piola-Kirchoff Stress tensor. To satisfy the 2nd Law of Thermodynamics and under the assumption of hyperelastic material, S is defined in reference to the strain energy function W as

$$S_{ij} = \frac{\partial W}{\partial F_{ij}} \tag{3.7}$$

3.2 Constitutive Model

In this analysis both the matrix and inclusion material are modeled as hyperelastic material. This model can be described using the following strain energy function

$$W(I_1, J) = \frac{\mu}{2}\left(\hat{I}_1 - 3\right) + \frac{K}{2}(J-1)^2 \tag{3.8}$$

where $\hat{I}_1 = J^{-\frac{2}{3}}\text{tr}(\mathbf{F}.\mathbf{F}^{\mathbf{T}})$ and $J = \det(\mathbf{F})$. The strain energy function is chosen to satisfy the material objectivity and laws of thermodynamics. A neo-Hookean model is used to describe the constitutive behavior of the hyperelastic material. The strain energy function is representative of Helmholtz free energy, and represents the elastically stored free energy per unit volume of rubber. The formulation is based on statistical mechanics of rubber, where the molecular chains are assumed to follow a Gaussian distribution [41]. While simplistic in nature, the neo-Hookean model captures the behavior of most rubber like material accurately, specifically those used in 3-D printing. applications[42].

- Stress versus strain relationship is governed by,

$$\mathbf{S} = \mu J^{\frac{-2}{3}}\mathbf{F} + J\left[K(J-1) - \frac{\mu}{3J}\hat{I}_1\right]\mathbf{F}^{-\mathbf{T}} \tag{3.9}$$

3.3 Wave Propagation

For the wave propagation problem, consider an incremental displacement imposed on a given prescribed displacement. These incremental deformations should satisfy the balance of linear momentum (BLM) governing the dynamic problem. Taking incremental displacement $\bar{u}$ in consideration yields,

$$\bar{S}_{ij,j} = \rho_o \ddot{\bar{u}}_i \tag{3.10}$$

where, $(^-)$ denotes incremental values. Considering only incremental deformations, it is convenient to also represent the stress and strain relationship through the stiffness moduli L_{ijkl} such that,

$$L_{ijkl} = \frac{\partial^2 W}{\partial F_{ij} F_{kl}} \tag{3.11}$$

from Eqn.3.8 and Eqn.3.11 we can compute the stiffness moduli;

$$\begin{aligned} L_{ijkl} = \mu J^{\frac{-2}{3}} \left[\delta_{ik}\delta_{jl} - \frac{4}{3}\delta_{il}\delta_{jk}\right] + \left[KJ(2J-1) + \frac{2}{3}\mu\hat{I}_1\right] F^{-1}_{ji} F^{-1}_{lk} - \\ \left[KJ(J-1) - \frac{\mu}{3}\hat{I}_1\right] F^{-T}_{il} F^{-T}_{kj} \end{aligned} \tag{3.12}$$

where, $I = \mathrm{tr}(F.F^T)$. We introduce the following definitions

$$\mathbb{J} = \frac{\partial F^{-T}_{ij}}{\partial F_{kl}} = -F^{-T}_{il} F^{-T}_{kj}, \qquad \mathbb{K} = \delta_{ik}\delta_{jl} - \frac{4}{3}\delta_{il}\delta_{jk}, \qquad \mathbb{A} = F^{-1}_{ji} F^{-1}_{lk} \tag{3.13}$$

Using the above definitions to rewrite the tangential stiffness moduli in a more compact form,

$$L_{ijkl} = \mu J^{\frac{-2}{3}} \mathbb{K} + \left[KJ(2J-1) + \frac{2}{3}\mu\hat{I}_1\right] \mathbb{A} - \left[KJ(J-1) - \frac{\mu}{3}\hat{I}_1\right] \mathbb{J} \tag{3.14}$$

It follows that for incremental displacements the stress-strain relationship can be written as,

$$\bar{S}_{ij} = L_{ijkl} \bar{F}_{kl} = L_{ijkl} \bar{u}_{k,l} \tag{3.15}$$

Starting from the equation of motion, the wave propagation problem is analyzed using Bloch wave analysis [43] and implemented in Finite element approach [44]. First consider a harmonic wave motion that corresponds to,

$$\bar{\mathbf{u}}(\mathbf{X}, t) = \bar{\Phi}(\mathbf{X})e^{-iwt} \tag{3.16}$$

with ω describing the frequency of vibration. It follows from stress being a function of $\mathbf{F}$ that the stress is also a complex valued field represented in a similar manner.

$$\bar{\mathbf{S}} = \bar{\mathbf{\Sigma}}e^{-iwt} \tag{3.17}$$

By substituting in the balance of linear momentum ,the equation is reduced to

$$\mathrm{Div}(\bar{\mathbf{\Sigma}})e^{-iwt} = \rho_o\omega^2\bar{\Phi}e^{-iwt} \tag{3.18}$$

To impose the periodicity of the structure, the incremental displacement is defined as,

$$\bar{\Phi_i} = \hat{\Phi}_i e^{ik_m X_m} \tag{3.19}$$

$$\bar{\Sigma}_{ij} = L_{ijkl}k_l\hat{\Phi}_k e^{ik_m X_m} \tag{3.20}$$

Inserting this into Eqn.3.18 yeilds

$$L_{ijkl}k_l k_j\hat{\Phi}_k = \rho_o\omega^2\hat{\Phi}_k \tag{3.21}$$

where k_l is the Bloch wave vector that conveys the direction of the wave propagation within the medium.

Furthermore, to properly satisfy the periodicity boundary condition any function $\mathcal{F}$ within the space of the problem is defined as such.

$$\mathcal{F}(\mathbf{X}) = \mathcal{F}(\mathbf{X} + \mathbf{L}) \tag{3.22}$$

Thus, substituting in Eqn.3.19 results in the following relation for the stress and deformation

$$\hat{\Phi}_i e^{ik_l X_l} = \hat{\Phi}_i e^{ik_l X_l} e^{ik_l L_l} \tag{3.23}$$

Leading to,

$$\hat{\Phi}(\mathbf{X}) = \hat{\Phi}(\mathbf{X} + \mathbf{L})e^{-i\mathbf{kL}} \tag{3.24}$$

The reciprocal lattice is mapped from the direct lattice and can be represented as a function of the base vectors $\mathbf{B}_1, \mathbf{B}_2$ in direct lattice. The mapping takes this form.

$$\mathbf{A}_1 = 2\pi \frac{\mathbf{B}_2 \times \mathbf{e}}{||\mathbf{B}_1 \times \mathbf{B}_2||}, \qquad \mathbf{A}_2 = 2\pi \frac{\mathbf{e} \times \mathbf{B}_1}{||\mathbf{B}_1 \times \mathbf{B}_2||} \tag{3.25}$$

with $\mathbf{e} = \frac{\mathbf{B}_1 \times \mathbf{B}_2}{||\mathbf{B}_1 \times \mathbf{B}_2||}$ such that

$$\mathbf{A}_i \mathbf{B}_j = 2\pi\delta_{ij} \tag{3.26}$$

Φ_i is a complex valued function that can be decomposed to a real part and imaginary part.

$$\hat{\Phi}_i = \hat{\Phi}_i^{Re} + i\hat{\Phi}_i^{Im} \tag{3.27}$$

The periodicity relationship is imposed on the stress strain model

$$\hat{\Phi}^{Re}(\mathbf{X}) = \hat{\Phi}^{Re}(\mathbf{X} + \mathbf{L})\cos(\mathbf{kL}) + \hat{\Phi}^{Im}(\mathbf{X} + \mathbf{L})\sin(\mathbf{kL}) \tag{3.28}$$

$$\Phi^{Im}(\mathbf{X}) = \hat{\Phi}^{Im}(\mathbf{X} + \mathbf{L})\cos(\mathbf{kL}) - \hat{\Phi}^{Re}(\mathbf{X} + \mathbf{L})\sin(\mathbf{kL}) \tag{3.29}$$

At this point It proves convenient to split all fields into real and imaginary parts. Thus the incremental BLM can be written as

$$\mathrm{Div}(\bar{\mathbf{\Sigma}}^{Re}) = \rho_o \omega^2 \bar{\Phi}^{Re}, \qquad \mathrm{Div}(\bar{\mathbf{\Sigma}}^{Im}) = \rho_o \omega^2 \bar{\Phi}^{Im} \tag{3.30}$$

Finite-element discretization of the given problem would then yield,

$$\left(\begin{bmatrix} \mathbf{K} & 0 \\ 0 & \mathbf{K} \end{bmatrix} - \omega^2 \begin{bmatrix} \mathbf{M} & 0 \\ 0 & \mathbf{M} \end{bmatrix} \right) \begin{bmatrix} \bar{\mathbf{u}}^{Re} \\ \bar{\mathbf{u}}^{Im} \end{bmatrix} = \begin{bmatrix} \bar{\mathbf{f}}^{Re} \\ \bar{\mathbf{f}}^{Im} \end{bmatrix} \tag{3.31}$$

where, $\mathbf{K}$ and $\mathbf{M}$ are the tangential stiffness and mass matrices respectively. To apply the periodicity constraint on the displacement, we define a connectivity matrix

that connects corresponding equivalent node pair a, b such that,

$$\bar{\mathbf{u}} = \begin{bmatrix} \bar{\mathbf{u}}^{Re} \\ \bar{\mathbf{u}}^{Im} \end{bmatrix} = \begin{bmatrix} \bar{\mathbf{u}}_i^{Re} \\ \bar{\mathbf{u}}_a^{Re} \\ \bar{\mathbf{u}}_b^{Re} \\ \bar{\mathbf{u}}_i^{Im} \\ \bar{\mathbf{u}}_a^{Im} \\ \bar{\mathbf{u}}_b^{Im} \end{bmatrix} = \mathbf{Q} \begin{bmatrix} \bar{\mathbf{u}}_i^{Re} \\ \bar{\mathbf{u}}_b^{Re} \\ \bar{\mathbf{u}}_i^{Im} \\ \bar{\mathbf{u}}_b^{Im} \end{bmatrix} \tag{3.32}$$

$\bar{u}_i$ indicates the interior nodes displacement and $\bar{u}_a$ and $\bar{u}_b$ are the equivalent boundary nodes, where $\mathbf{Q}$ is defined as such

$$\mathbf{Q} = \begin{bmatrix} \mathbf{I} & 0 & 0 & 0 \\ 0 & \cos(\mathbf{kL}) & 0 & \sin(\mathbf{kL}) \\ 0 & \mathbf{I} & 0 & 0 \\ 0 & 0 & \mathbf{I} & 0 \\ 0 & -\sin(\mathbf{kL}) & 0 & \cos(\mathbf{kL}) \\ 0 & 0 & 0 & \mathbf{I} \end{bmatrix} \tag{3.33}$$

The elastic wave propagation problem can then be evaluated by solving an eigenvalue problem.

$$\mathbf{Q^T} \left(\begin{bmatrix} \mathbf{K} & 0 \\ 0 & \mathbf{K} \end{bmatrix} - \omega^2 \begin{bmatrix} \mathbf{M} & 0 \\ 0 & \mathbf{M} \end{bmatrix} \right) \mathbf{Q} = \mathbf{0} \tag{3.34}$$

In a more compact form;

$$\bar{\mathbf{K}} - \omega^2 \bar{\mathbf{M}} = 0 \tag{3.35}$$

The problem is solved in an in-house code to find the frequencies of elastic wave propagation for varying wave vectors k. The computational effort involved in solving this problem is substantially reduced through implementing Craig-Bampton method to condense the degree of freedoms associated with the interior nodes.

3.4 Finite Element Setup

The behavior of the fibril with soft inclusion is studied using finite element simulations. The simulations provide significant insight on the response of the fibril to large elastic deformations both before and post buckling. In this section, the problem definitions that govern the numerical simulations presented in this thesis are demonstrated.

3.4.1 Geometry

A polymer fibril with total length L and width h is considered. The fibril contains patterned inclusions. The inclusion is of length L_i and width t. The unit cell used in this study is presented in Fig.3.1. The length L of the unit cell is 290 μm, the depth h is 30 μm, S is 35 μm, t is 4 μm, L_i is 40 μm, and the distance between the rows c is 16 μm. The dimensions are chosen arbitrarily since the elastic problem described is independent of the scale. The impact of the geometric parameters will be thoroughly studied to identify its effect on the behavior of the fibril. In our analysis, the length scale used is μm and the stress scale is GPa.

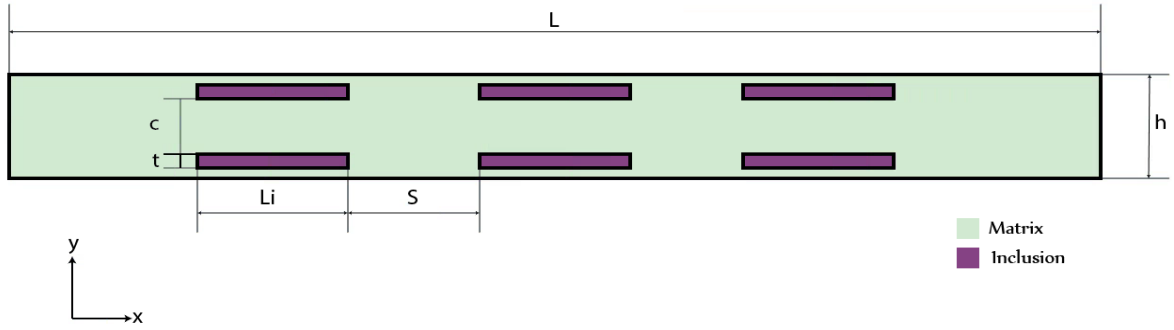

Figure 3.1: Material model of the proposed composite material, showing the stiff matrix material and soft inclusions. The geometry of inclusion is defined through the thickness t and length L_i, the patterning is defined by the horizontal spacing S and vertical spacing c, with overall composite length L and height h.

3.4.2 Material Properties

For the hyperelastic constitutive model used, the matrix material is considered the stiff constituent with Young's modulus of E_m=0.5 GPa, Poisson's ratio of v_m=0.495, and bulk density of ρ_m=2000 kg/m^3, which is similar to that of collagen fibrils [45]. The stiffness of the inclusion varies throughout our discussion, the inclusion stiffness is described by the stiffness ratio, that is the ratio between the matrix stiffness and inclusion stiffness (E_m/E_i). The density of the inclusion is chosen as ρ_i=1400 kg/m^3.

3.4.3 Numerical Model

The FEM software Abaqus [46] is used in the numerical analysis of the model. 8-node biquadrilateral elements are used in the model. The study is considered for a generalized plane-stress domain using a quasi-static analysis. Geometric non-linearities is considered throughout this analysis. A full newton scheme is used to compute the displacement field.

3.4.4 Loading Conditions

Prior to buckling, the problem is considered as uniaxial compression in the direction of the principle axis of the fibril. The load is applied through a prescribed end-shortening u. During this quasi-static analysis, the ends of the fibril are restricted to move in the horizontal direction only. End shortening is applied on both ends equally and in opposite directions. The displacement is applied incrementally with rate $\dot{u} = -2 \times 10^{-7}$ $\mu m/s$, which is small enough to render any inertia effects negligible and to ensure convergence of the nonlinear solver.

$$u_x(r, y) + u_x(l, y) = u, \qquad u_y(r, y) = u_y(r, y) = 0 \tag{3.36}$$

where r and l denote the right and left edges of the fibril, respectively. For band gap evolution of the composite, Bloch-periodicity is imposed at the two ends of the fibril. We further add a roller to remove instabilities that might occur due to the relaxation

of the model. Eqn.3.37 defines the Bloch periodicity boundary conditions.

$$\bar{u}_x(r,y) = \bar{u}_x(l,y)e^{-ikL}, \qquad \bar{u}_y(r,y) = \bar{u}_y(l,y)e^{-ikL}, \qquad \bar{u}_y(r,0) = \bar{u}_y(l,0) = 0 \tag{3.37}$$

CHAPTER 4

NON-LINEAR VARIATIONAL ANALYSIS

To evaluate the behavior of the fibril post global buckling, local instabilities and the global buckling of the fibril are considered separately. First, the global buckling of a fibril under axial compression is considered through Euler elastica, then the local instability happening in the fibril is isolated and treated as a problem of a beam resting on an elastic foundation and solved using variational analysis. The overall interaction between the global and local buckling contributes to a global negative post-buckling stiffness. The results presented here are complemented by conducting FEM simulation for the overall response of a fibril with soft inclusions in Chapter 5.

4.1 Global Buckling

The global buckling of the fibril can be approximated by elastica formulation, as shown in Fig.4.1, based on the fact that the fibril aspect ratio is very small. The strain energy function is reduced to the following form as a function of the end deflection.

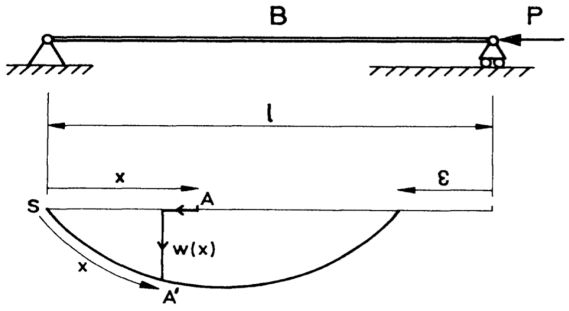

Figure 4.1: The fibril under axial compression P and transverse displacements $w(x)$ [47].

The deflection of the beam is based on the transverse deformation $w(x)$ and the curvature θ of the beam given by the following relation,

$$\theta = \frac{d}{dx}\sin^{-1}(\frac{dw}{dx}) = \frac{d^2w}{dx^2}\left[1 - \left(\frac{dw}{dx}\right)^2\right]^{-0.5} \tag{4.1}$$

The total energy in the system is given by the strain energy U due to the rotation of the beam minus the applied load energy Pu. Where u is the applied end shortening.

$$V = U - Pu \tag{4.2}$$

The strain energy and the axial end shortening can be described in terms of the transverse deflection accordingly

$$U = \frac{1}{2}\int_0^l EI\theta^2 \tag{4.3}$$

$$u = l - \int_0^l \left[1 - \left(\frac{dw}{dx}\right)^2\right]^{0.5} dx \tag{4.4}$$

Now consider the total energy

$$V = \frac{1}{2}\int_0^l EI\left[\frac{d^2w}{dx^2}\right]^2\left[1 - \left(\frac{dw}{dx}\right)^2\right]^{-1} dx - P\left[l - \int_0^l \left[1 - \left(\frac{dw}{dx}\right)^2\right]^{0.5}\right] dx \tag{4.5}$$

$$V = \frac{1}{2}\int_0^l EI\left[\frac{d^2w}{dx^2}\right]^2\left[1 - \left(\frac{dw}{dx}\right)^2\right]^{-1} dx - P\left[\int_0^l 1 - \left[1 - \left(\frac{dw}{dx}\right)^2\right]^{0.5}\right] dx \tag{4.6}$$

$$V = \int_0^l F(w'', w')dx \tag{4.7}$$

We observe the above functional is in terms of w'' and w', where the prime is used to denote the derivative with respect to x. We can implement Hamilton's principle to obtain the governing equation for the deformation of the beam.

$$\frac{d^2}{dx^2}\frac{\partial F}{\partial w''} - \frac{d}{dx}\frac{\partial F}{\partial w'} = 0 \tag{4.8}$$

Alternatively, the bifurcation load can be obtained by minimizing the total potential energy functional V in terms of the displacements to obtain the value of P that causes global buckling. The linear version of this equation is the Euler elastica, which indicates that the beam will buckle with deformation modes equivalent to a sine wave that satisfies the imposed boundary condition.

$$w(x) = A\sin(\frac{n\pi x}{l}) \qquad n = 1, 2, \ldots \tag{4.9}$$

In the case of small deformations, the buckling load is then given by the following relationship;

$$P_{cr} = \frac{\pi^2 EI}{l^2} \tag{4.10}$$

For this specific problem, considering small perturbation beyond the critical load, it is observed that the post-buckling behavior is stable in nature [48]. It was shown that the post-bifurcation stiffness E_t of an incompressible bar is given through Eqn.4.11, and shown in Fig.4.2

$$E_t = E\frac{\pi^2 i^2}{2l^2} \tag{4.11}$$

Where, $i = \sqrt{(I/A)}$ is the radius of gyration of the corss section.

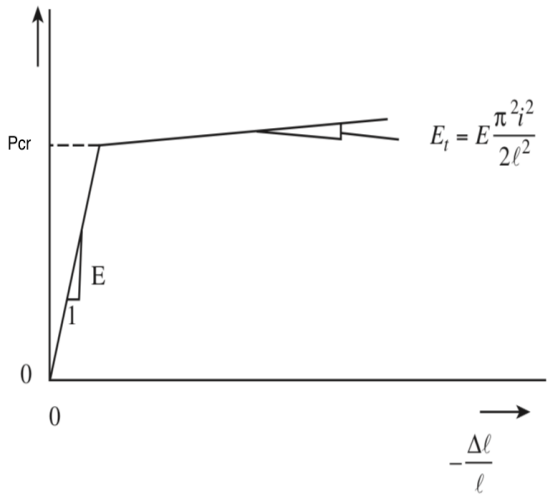

Figure 4.2: Post-bifurcation behavior of an incompressible bar demonstrating positive post-buckling stiffness (stable system) [48].

4.2 A Semi-analytical Model: Beam on Elastic Substrate

To unravel the origin of the negative post-buckling stiffness, the following semi-analytical approach is presented. We idealize the rib that undergoes local buckling as a beam resting on an elastic substrate and the soft inclusion is idealized as an elastic substrate providing resistance to transverse displacement. This is described in a finite deformation sense through the following strain energy presented in Eqn.4.12, which is a function of the rotations, Cauchy-Green strain ϵ_{xx} associated with axial deformations, and energy contribution due to the traverse motion on an elastic foundation

$$V = \frac{1}{2}\int_0^{L_i} EI\theta^2 - P\epsilon_{xx}^2 + kw(x)^2 dx \tag{4.12}$$

where k is the effective modulus of the elastic foundation and L_i is the length of the idealized rib.

The solution of the beam on an elastic foundation is done in a two step process; the deformation of the rib is computed using the linearized version of the governing equation and then used as an admissible solution for the non-linear problem. Expanding the derivatives in terms of transverse displacement $w(x)$, Eqn.4.12 becomes;

$$V = \frac{EI}{2}\int_0^{L_i} w(x)_{,xx}^2/(1+w(x)_{,x}^2)dx - P\int_0^{L_i}\left[1-(1-w(x)_{,x}^2)^{0.5}\right]dx + \frac{k}{2}\int_0^{L_i} w(x)^2 dx \tag{4.13}$$

The functional U is normalized through introducing the following quantities

$$\lambda = \left(\frac{4EI}{k}\right)^{\frac{1}{4}} \qquad \sigma = \frac{P\lambda^2}{4EI} \qquad \zeta = \frac{w}{\lambda} \qquad \eta = \frac{x}{\lambda} \tag{4.14}$$

such that λ is a length scale, and σ is P/P_{cr}, with P_{cr} being the critical buckling load $4EI/\lambda^2$. Accordingly, Eqn.4.13 can be rewritten in its normalized form.

$$V = (\frac{EI}{2\lambda})\left(\int_0^{L_i/\lambda}\zeta(\eta)_{,\eta\eta}^2/(1-\zeta(\eta)_{,\eta}^2)d\eta - 8\sigma\int_0^{L_i/\lambda}\left[1-\left(1-\zeta(\eta)_{,\eta}^2\right)^{\frac{1}{2}}\right]d\eta + \int_0^{L_i/\lambda} 4\zeta(\eta)^2 d\eta\right) \tag{4.15}$$

Through the quadratic terms in the potential energy, one can find the governing

equation for the linearized problem using Hamilton's principle.

$$\zeta(\eta)_{,\eta\eta\eta\eta} + 4\sigma\zeta(\eta)_{,\eta\eta} + 4\zeta(\eta) = 0 \tag{4.16}$$

We assume that the beam is fixed at the ends, that is, the local rib is restrained at both ends due to its embodiment in the matrix material. Accordingly, the boundary conditions reduce to:

$$\zeta(0) = 0 \qquad \zeta(\frac{L_i}{\lambda}) = 0 \qquad \zeta(0)_{,\eta\eta} = A \qquad \zeta(\frac{L_i}{\lambda})_{,\eta\eta} = A \tag{4.17}$$

where A is an arbitrarily applied normalized end moment. The above boundary value problem admits a closed form solution based on the value of σ. This evaluation is based on solving the eigen-form of the problem and obtaining the roots of the solution. For this biquadractic equation there exists four roots; periodic solutions are only admissible if $\sigma \geq 1$. The first and smallest critical buckling load is thus achieved at $\sigma = 1$. The buckling mode takes the following form:

$$\zeta(\eta) = \frac{A\sec^2\left(\frac{L_i}{\sqrt{2}\lambda}\right)\left(\sin\left(\sqrt{2}\eta\right)(\eta\lambda - L_i) + \eta\lambda\sin\left(\frac{\sqrt{2}(\eta\lambda - L_i)}{\lambda}\right)\right)}{4\sqrt{2}\lambda} \tag{4.18}$$

The displacement mode shown in Eqn.4.18 is used as an admissible function for a one-term Rayleigh-Ritz approximation to minimize the strain energy function.

$$\min_A \left[(\frac{EI}{2\lambda})\left(\int_0^{L_i/\lambda} \zeta(\eta)^2_{,\eta\eta}/(1-\zeta(\eta)^2_{,\eta})d\eta - 8\sigma\int_0^{L_i/\lambda}\left[1-\left(1-\zeta(\eta)^2_{,\eta}\right)^{\frac{1}{2}}\right]d\eta + \int_0^{L_i/\lambda} 4\zeta(\eta)^2 d\eta\right)\right] \tag{4.19}$$

Eqn.4.19 serves as a starting point for the study of the post-buckling response of a beam resting on an elastic foundation. The solution of the problem depends on perturbing the amplitude of the displacement. Applying Taylor series expansion on

some of the terms in Eqn.4.19 yields.

$$V = \frac{EI}{2\lambda}\left(\int_0^{L_i/\lambda} \zeta(\eta)^2_{,\eta\eta}(1+\zeta(\eta)^2_{,\eta}+\zeta(\eta)^4_{,\eta}+\dots)d\eta - 8\sigma\int_0^{L_i/\lambda}\left[\frac{\zeta(\eta)^2_{,\eta}}{2}+\frac{\zeta(\eta)^4_{,\eta}}{8}+\dots\right]d\eta + \int_0^{L_i/\lambda} 4\zeta(\eta)^2 d\eta\right) \tag{4.20}$$

Considering only quadratic terms would yield the linearized version of the problem, the non-linearities are attributed to higher order terms. In the limit of small perturbations, the contribution of higher order terms above the fifth are negligible, and can be consistently disregarded [49]. In our analysis, terms up to the 6^{th} order are considered, thus yielding;

$$V = \frac{EI}{2\lambda}\left(\int_0^{L_i/\lambda} \zeta(\eta)^2_{,\eta\eta}(1+\zeta(\eta)^2_{,\eta}+\zeta(\eta)^4_{,\eta})d\eta - 8\sigma\int_0^{L_i/\lambda}\left[\frac{\zeta(\eta)^2_{,\eta}}{2}+\frac{\zeta(\eta)^4_{,\eta}}{8}+\frac{\zeta(\eta)^6_{,\eta}}{16}\right]d\eta + \int_0^{L_i/\lambda} 4\zeta(\eta)^2 d\eta\right) \tag{4.21}$$

The derivatives of the displacement is then substituted in Eqn.4.21 and integrated over the domain L_i/λ. The energy is minimized by considering $\partial V/\partial A = 0$ and then solving for the post-bifurcation normalized load σ in terms of amplitude A.

4.3 Foundation Modulus

The modulus of the substrate is computed through $p_r = kw(x)$, where p_r is the distributed reaction of the foundation against the rib. This analysis is done numerically using the finite element model shown in Fig.4.3. Four different stiffness ratios are considered (SR=25, 50, 100, and 200), the corresponding Foundation modulus k is demonstrated in Fig.4.4 showing k values of 3.8, 3.2, 2.6, and 1.9 GPa, respectively.

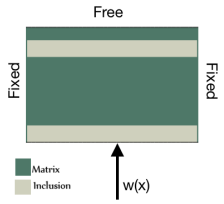

Figure 4.3: Model and boundary conditions being investigated to compute the value of the foundation modulus c, the reaction force $p(x)$ is computed toward the applied displacement $w(x)$.

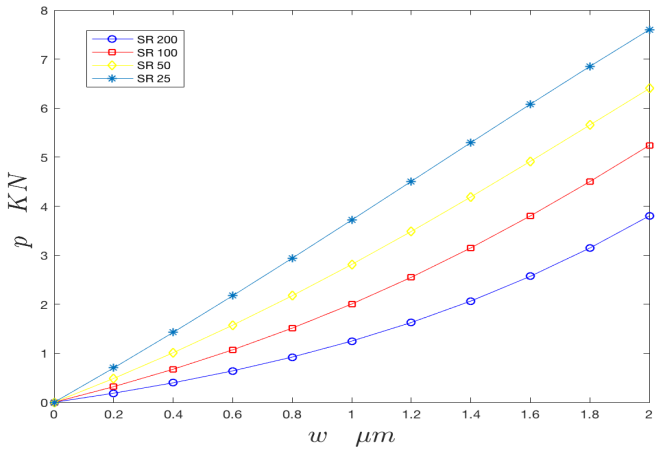

Figure 4.4: The reaction forces $p(x)$ versus the transverse displacement $w(x)$ for different inclusion stiffness of SR=25, 50, 100 and 200. The corresponding foundation coefficient k is 3.8, 3.2, 2.6 and 1.9 GPa, respectively.

4.4 Post-buckling Behavior of Beams on an Elastic Foundation

From the foundation modulus obtained in Sect. 4.2, the length scale is computed to be $\lambda = 6.45$ for SR=100, and using the parameters provided in Chapter 2. The deformation mode is computed from Eqn.4.18. Finally, through minimization the values for σ, post-buckling is computed in terms of A. We further note that the amplitude A is monotonically increasing with the end shortening. The relationship between A and σ is presented in Fig.4.5, which demonstrates that for a beam resting on an elastic substrate, the post-buckling behavior is unstable in nature, given the

assumption that the soft inclusion is modeled with constant transverse stiffness. While in this approximate analysis, the stiffness of the substrate term is assumed constant, it should be noted that in the full model setup, the local rib is resting on a soft non-linear hyperelastic material which is in turn resting on a stiffer material (the matrix). That is, the transverse stiffness supporting the rib is composed of a series of different layers suggesting that the thickness of the inclusion should play a role in the analysis, as will be discussed shortly. Furthermore, it is intuitive to realize that should the stiffness of the inclusion approaches that of the fibril, the local instability will vanish.

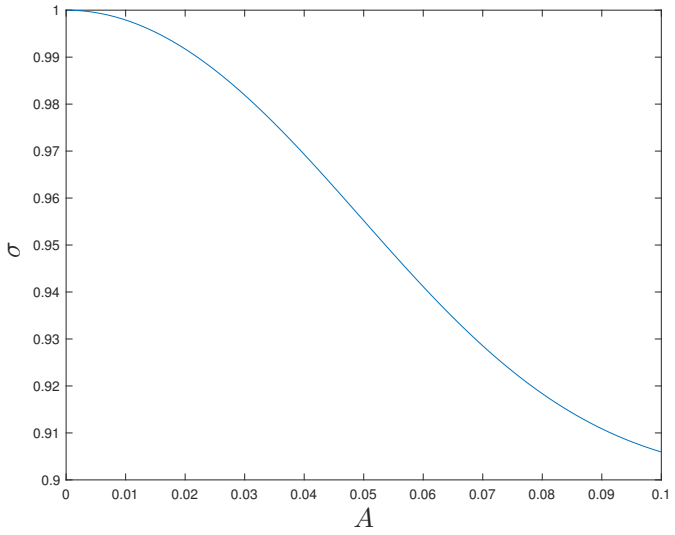

Figure 4.5: Post-buckling relationship between amplitude A and σ obtained through the perturbation of amplitude A, where $\sigma = 1$ indicates the buckling load of the rib in the non-linear analysis.

4.5 Impact of Varying Foundation Modulus k

In the above analysis, the results are limited to a single k value. In order to be comprehensive, it is critical to assess the influence of the inclusion parameters. We take as an example, the effect of substrate modulus. The different foundation modulus for various inclusion SR is computed using the finite element model shown in Sect.4.3. Fig.4.6 presents the relationship between the normalized stiffness ($d\sigma/dA$), and the

perturbed amplitude A to demonstrate the impact of varying foundation modulus. For the various substrate modulus, a negative post-buckling slope is still observed. However, a non-monotonic response exists where initially as the stiffness of inclusion is increased, the negative slope is larger in amplitude. However, when the stiffness is further increased, a reduction in the negative stiffness value is obtained.

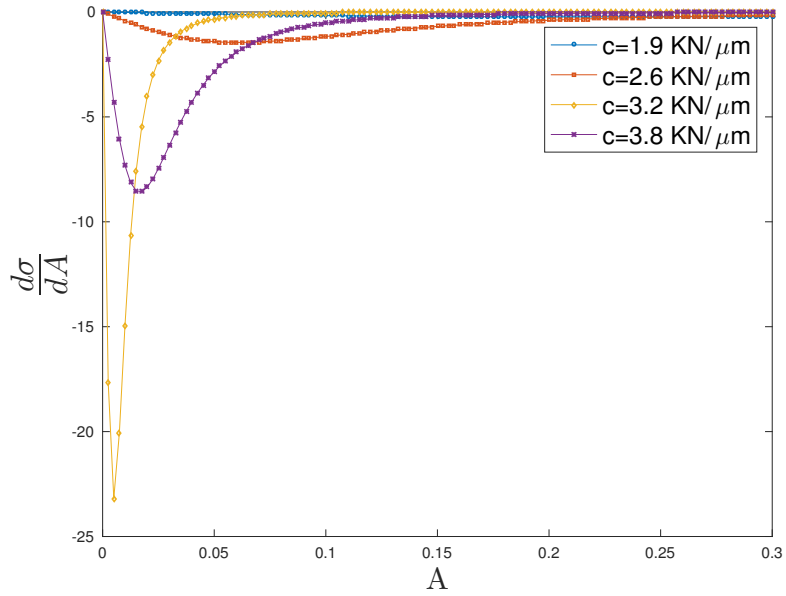

Figure 4.6: Post-buckling stiffness relationship between amplitude A and σ obtained through the perturbation of amplitude A, where $\sigma = 1$ indicates the buckling load of the rib in the non-linear analysis.

CHAPTER 5

POST-BUCKLING RESPONSE OF FIBRILS WITH SOFT INCLUSION

In this chapter, we present the results of the finite element simulations to demonstrate the role of different inclusion parameters on the post-buckling response of the fibril. We also include a case where the stiffness of the inclusion becomes zero, idealizing a void, for comparison purposes.

5.1 Reference Case

Fig.5.1a, outlines the four different stages of compression the fibril undergoes. The magnitude of the displacement is presented to illustrate these different stages. Initially, the fibril is undergoing axial compression. When the composite reaches the critical load, it starts to buckle and the compressive stresses are localized in the bottom rib of the composite. This localization of stress results in local buckling in the rib that is resting on the softer inclusion. Following the stability analysis outlined in Section 3, we expect that the post-buckling stiffness of the rib is negative. This is indeed verified by the numerical simulations. In the post buckling regime, as shown in Fig.5.1b, the slope of the force-displacement curve is negative. With further loading, the slope starts to decrease and then stagnates. Fig.5.2 shows the stress concentrations prior to buckling and post-buckling, demonstrating the localization that contributes to the instability of the rib. Through out the analysis the stresses do not exceed the tensile stress of collegan fibrils [50]. Fig.5.3 details the formation of the wrinkle: as the rib buckles and the soft inclusion elongate reaching to 33% at 13 μm end shortening, the strain localized within the inclusion does not exceeds the failure limits of elastomeric material.

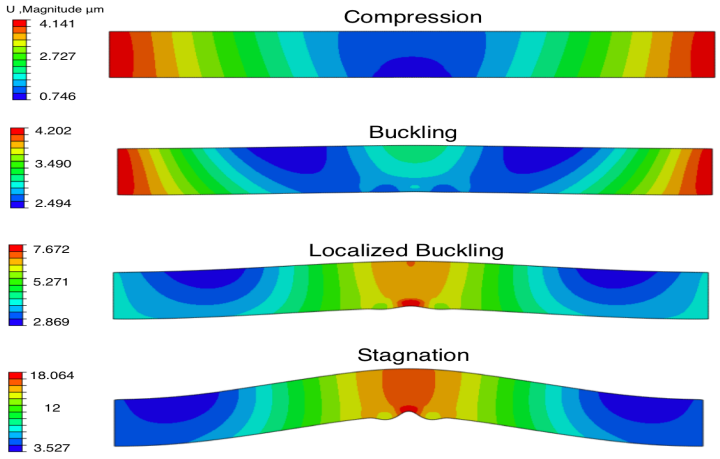

(a)

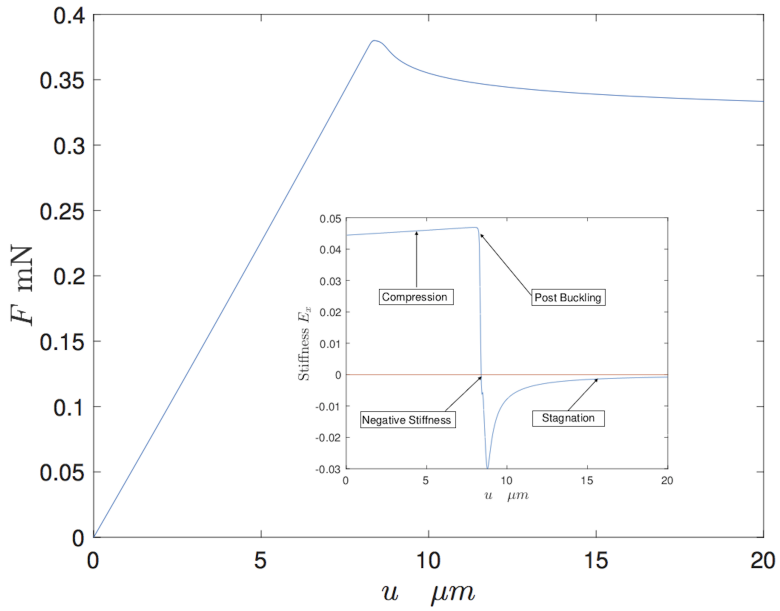

(b)

Figure 5.1: Response of composite fibril to end shortening (a) different stages of compression, starting with contraction, then buckling which induces localized instabilities, eventually stagnation, (b) the reaction force versus and the end-shortening showing negative post-buckling slope and stagnation phases.

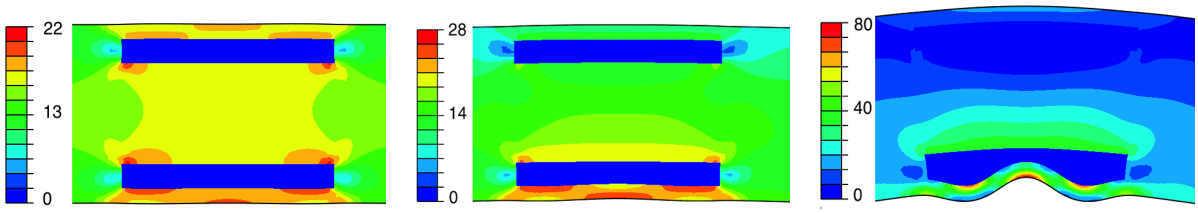

(a) (b) (c)

Figure 5.2: Von mises stress distribution in MPa inside the fibril as end shortening is applied: (a) fibril right before buckling occurs with stress distributed in the entirety of the fibril around the top and bottom rib, (b) post-buckling response with localization of stress around the bottom rib which causes instability, and (c) the stagnation response with the emergence of wrinkles.

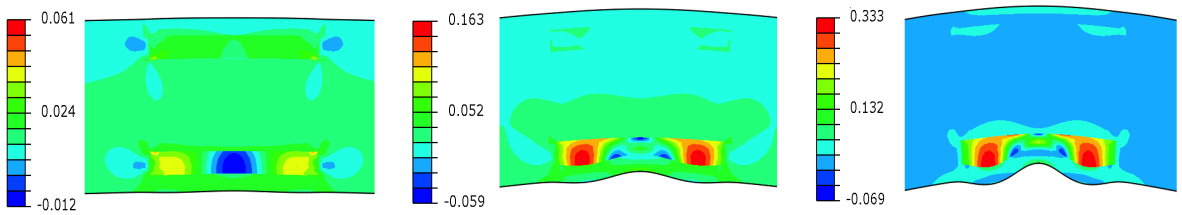

(a) End shortening 8 μm (b) End shortening 10 μm (c) End shortening 13 μm

Figure 5.3: Maximum in-plane elastic strain under various end shortening showing the increase in elongation in the inclusion due to the progressive localized buckling; at 13 μm end shortening, the elastic strain reaches 33%.

5.2 Mesh Sensitivity

To ensure mesh independence from the solution obtained from the finite element simulations, a mesh sensitivity analysis is conducted on the results obtained for the reference case shown in Fig.3.1 for the same material properties and geometry. Two cases are considered, first the impact of refinement on critical buckling load, then the impact of refinement on a slightly perturbed load at 10 μm end shortening. The aim is to obtain an optimal mesh size such that the solution accuracy is not compromised as well as minimize the computational cost of the simulations. Another important

factor in the choice of the mesh size is the spacing between the inclusion and the surface of the fibril.

Fig.5.4 demonstrates that as the mesh size decreases the buckling load and the post-buckling load converge to the solution. Furthermore, the buckling load varies 0.002 KN in magnitude as the mesh is refined from 1 μm to 0.5 μm. It is noted that at 1.5 μm mesh size the refinement is sufficient to capture the exact behavior of the rib resting on the soft substrate. For computational efficiency, a mesh size of 1 μm is utilized in our static analysis.

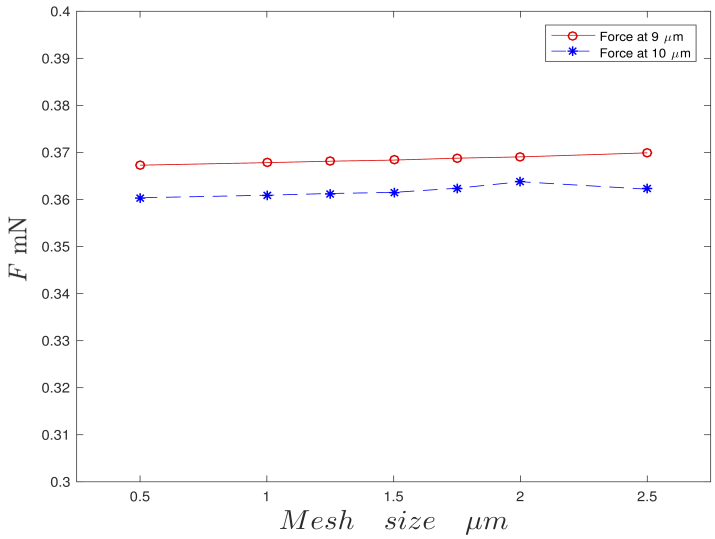

Figure 5.4: Mesh refinement influence on the post-buckling behavior of the composite fibril.

5.3 Effect of Inclusion Thickness and Row Spacing

In this section the post-buckling response of the fibril is evaluated with varying width of the inclusion. We consider inclusion thickness t of 2, 4, 6, and 8 μm and row spacing c of 20, 16, 12, and 8 μm. In these cases, the width of the inclusion is fixed at L_i=40 μm and only the thickness t is changed. The post-buckling response in each case is examined to quantify the impact of the inclusion width on the post-buckling slope. The resulting buckling shape is also presented to evaluate the influence of the inclusion on the surface profiles of the buckled fibril and the emergence of wrinkles.

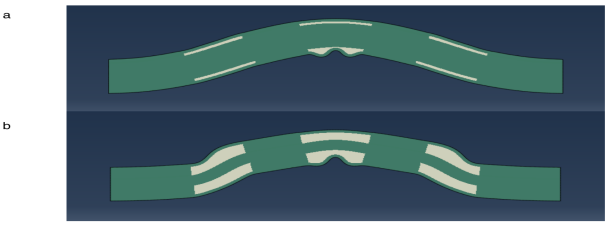

Figure 5.5: Buckled shape of two difference cases: (a) case 1 with the thickness of the inclusion equal to 2 μm, and (b) case 2 with the thickness of the inclusion equal to 8 μm.

Fig.5.6 summarizes the effect of the inclusion thickness on the buckling response of the fibril. As the thickness of the inclusion increases, the overall stiffness of the fibril decreases. Accordingly, the fibril buckles at lower load. The overall horizontal stiffness of the composite demonstrated in Fig.5.6a further illustrates such behavior.

Fig.5.6b shows that as the inclusion thickness increases, the post-buckling response of the fibril approaches that of a homogeneous problem, and the negative stiffness is no longer observed. On the other hand, when the inclusion thickness is very small (e.g. t=2 μm), the adjacent rib requires higher compressive force to initiate localized buckling, thus causing the delay in the negative stiffness response. This is further observed in Fig.5.6a, where the structural stiffness starts to drop initially, yet maintains a stable post-buckling behavior. However, as soon as the localized instabilities start to develop, the stiffness drops into the negative regime and then an unstable post-buckling behavior is observed.

The buckled shape of the fibril is examined for the two extreme cases with t=2 μm and t=8 μm, as presented in Fig.5.5. For the first case shown in Fig.5.5a, we observe in the bottom surface of the fibril an emergence of wrinkles at the mid span, and the top surface resembles that of the homogeneous case. Case 2, shown in Fig.5.5b, demonstrates that when the inclusions are thicker, there is an emergence of a folding behavior due to the bending at the edge inclusions. This folding behavior describes a deviation from the smooth surface profiles usually associated with the buckling modes. It is observable that the fibril with the inclusion thickness of 2 μm is experiencing a special case where the unstable buckling response is delayed. If we track the post-buckling deformation progress of this special case in Fig.5.6a, it is clear that global buckling is not directly followed by localized modes, but rather

the fibril proceeds to buckle globally and, consequently, the fibril remains in the stable region. Further loading of the fibril results in localized effects which induce the unstable behavior.

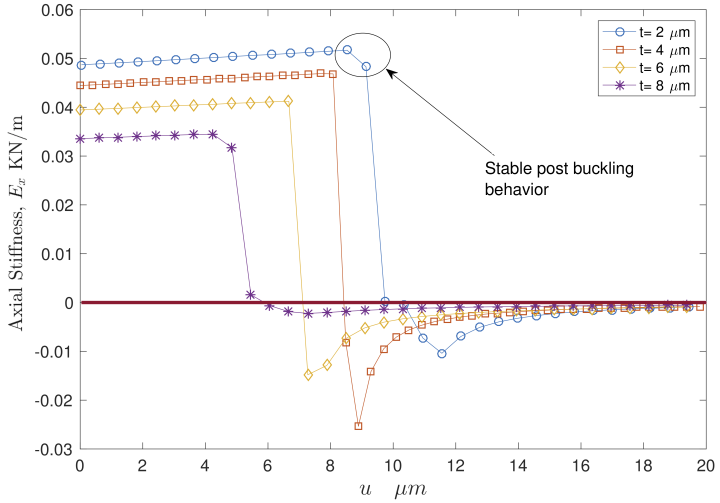

(a)

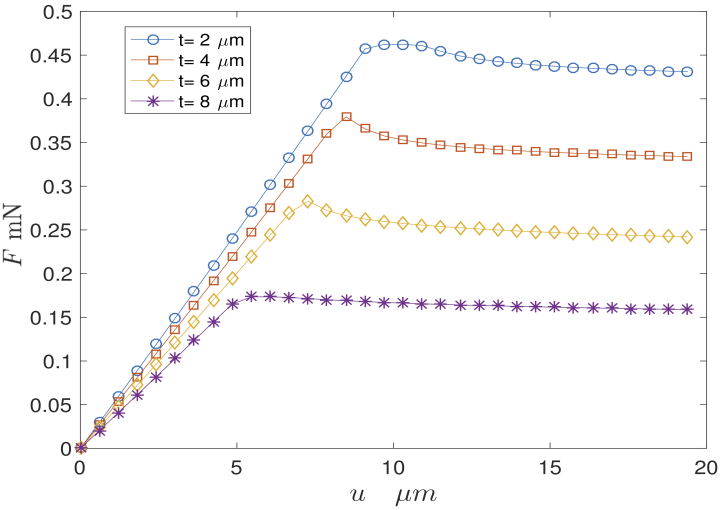

(b)

Figure 5.6: Post-buckling response of composite fibril with four different inclusion thickness: (a) progressive loading of composite fibril demonstrating the relationship between the end-shortening and the resulting reaction force in longitudinal x-direction, and (b) longitudinal stiffness representation through the reaction force vs. end shortening slope for various inclusion thicknesses.

5.4 Effect of Inclusion Length

Fig.5.7 shows the force versus end-shortening relationship when the inclusion length is varied. Four cases are considered with L_i=40, 60, 70 and 80 μm. The critical buckling load decreases with the increased volume fraction of soft inclusion (i.e. increasing the inclusion length). Furthermore, it is worth noting that the localized buckling behavior depends vastly on the distribution of inclusions within the matrix, since for the fibrils with the longer ribs, the localized effects do not emerge on the onset of global buckling. However, the post-local buckling stiffness is approximately the same across the different cases.

The buckling mode shown in Eqn.4.18 is directly correlated with the length; this dependency captures the additional flexibility added to the model through the increase in length of the rib. Accordingly, for a similar wavelength, a longer fibril would yield more wrinkles. Numerically, this is shown to be the case as illustrated in Fig.5.8.

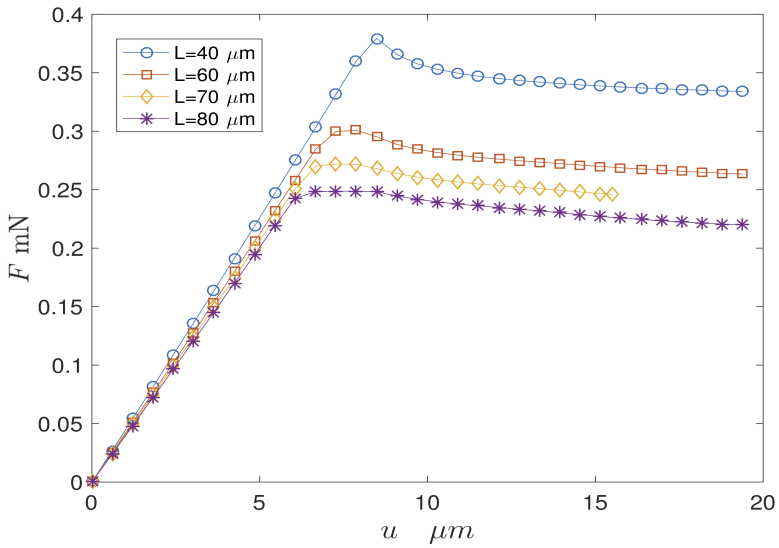

Figure 5.7: Effect of L_i on the load versus end-shortening.

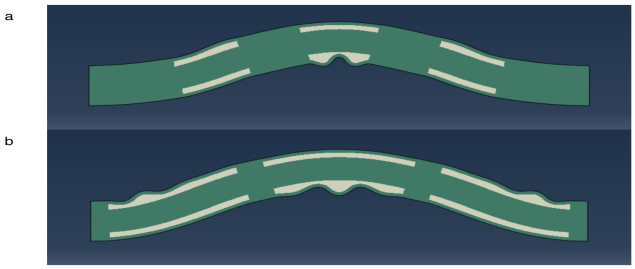

Figure 5.8: Buckled shape of two difference cases: (a) case 1 with the length of the inclusion equal to 40 μm, and (b) case 2 with the length of the inclusion equal to 80 μm.

5.5 Effect of Stiffness Ratio

Fig.5.9a shows the influence of the stiffness ratio on the composite force displacement response for four different stiffness ratios (E_m/E_i) 50, 100, 250, and 500. The buckling occurs at lower load for materials with higher stiffness ratio. The onset of local buckling is also delayed for a higher stiffness ratio.

Fig.5.9b suggests that the maximum value of the negative stiffness in the post-buckling regime does not vary monotonically with the stiffness ratio. In particular, the peak negative stiffness initially increases with increasing stiffness ratio up to a critical value and then decreases again. This agrees qualitatively with the predictions of the semi-analytical model shown in Fig.4.6. This response may be understood as follows. If the stiffness of the inclusion is zero, there is no resistance to the local buckling of the rib and the post-buckling stiffness in non-negative. As the stiffness of the inclusion increases, its resistance to the rib transverse displacements increases, leading to higher modes of local buckling and increased apparent negative stiffness. If the stiffness of the inclusion approaches that of the matrix, the overall fibril approaches the homogeneous limit. In this case, the post-buckling stiffness becomes non-negative again.

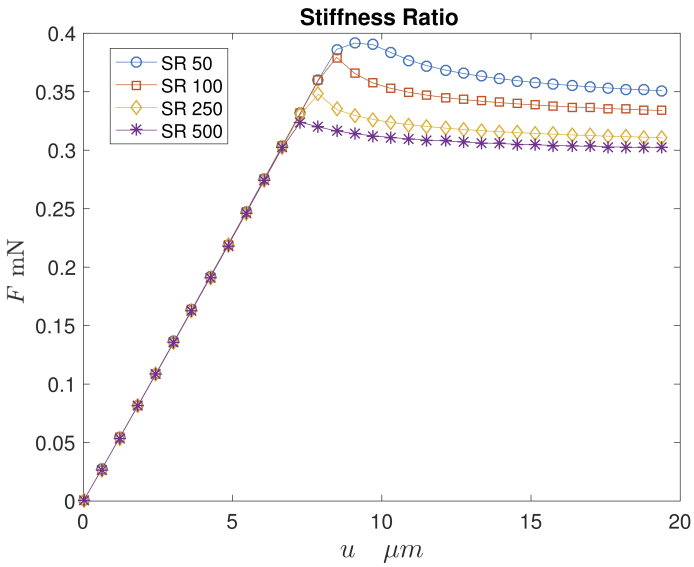

(a)

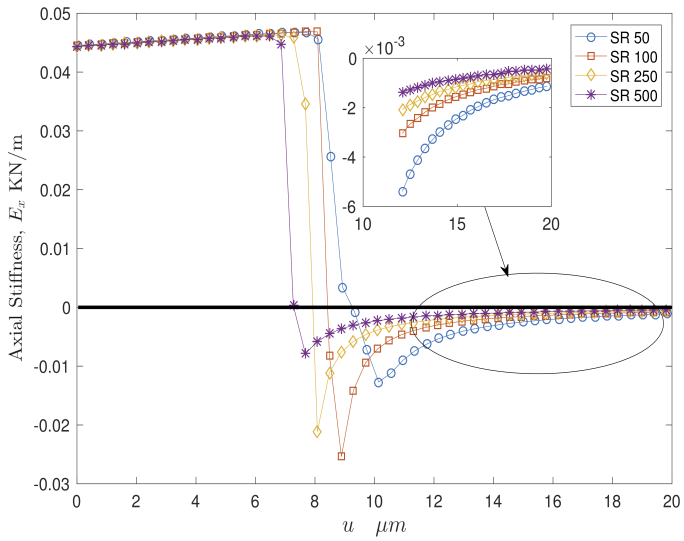

(b)

Figure 5.9: Post-buckling response of composite fibril with four different stiffness ratios: (a) progressive loading of composite fibril demonstrating the relationship between the end-shortening and the resulting reaction force in longitudinal x-direction, and (b) longitudinal stiffness representation through the reaction force vs. end shortening slope for various stiffness ratios.

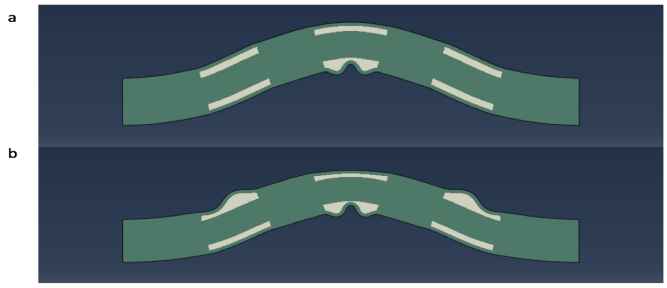

Figure 5.10: Buckled shape of two difference cases: (a) a composite fibril with stiffness contrast of 50, and (b) composite fibril with stiffness contrast of 500.

5.6 Special Case: Voids

To evaluate the limit of the stiffness of the inclusion goes to zero, let us consider a case of a fibril with voids having the same dimensions as the inclusions in the reference model. Initially the material is being compressed and the ribs that are not supported undergo transverse deflection. Further end shortening induce global buckling in the entire fibril.

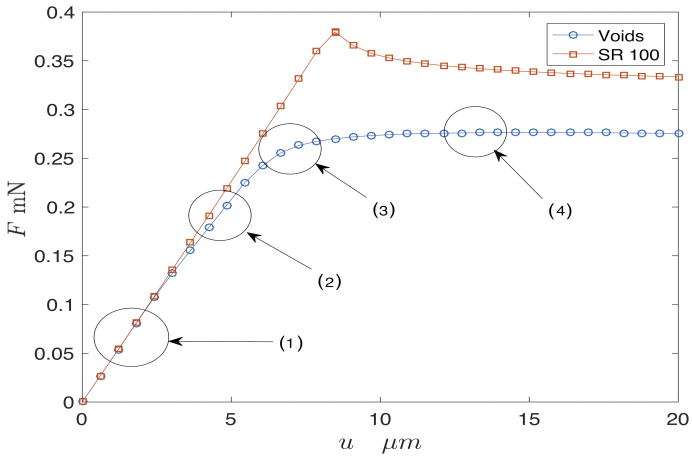

Figure 5.11: The Response of fibril with soft inclusions compared to fibril with voids demonstrating the impact of the inclusion in producing negative post-buckling stiffness.

For the post buckling response, Fig.5.11 demonstrates that the fibril does not experience negative post-buckling stiffness. We attribute that to the absence of the transverse stiffness component, which induces the unstable post-buckling response.

That is, if we consider the limit that $k \to 0$, it is expected that the local buckling mode will have a stable bifurcation similar to the global buckling mode, yielding an overall postive post-buckling stiffness. This complements the findings in Sect. 5.5. Fig.5.12 illustrates the deformation stages of the fibril.

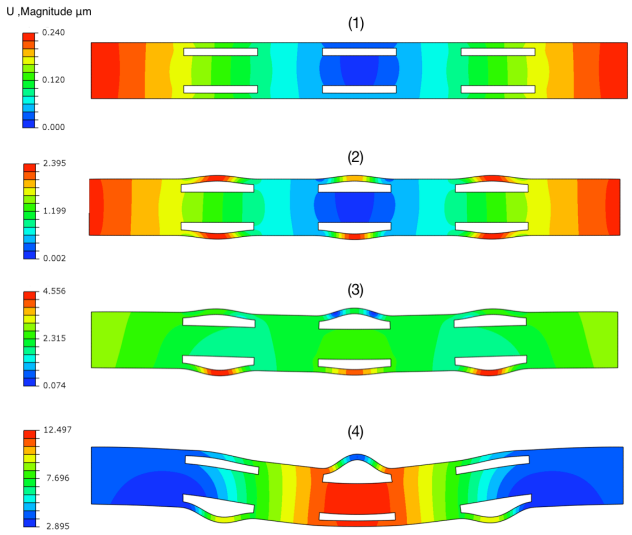

Figure 5.12: The progressive deformation of voided fibril showing the its different stages of (1) initial configuration, (2) post initial compression with the ribs deflecting in the transverse direction, (3) the onset of buckling, and (4) fully buckled fibril.

5.7 Varying Deformed Surfaces

In this section, the alternative deformation modes attainable for a buckled fibril with soft inclusions are discussed. The goal of this section is to provide alternatives for material design and demonstrate the capabilities of fibrils with soft inclusions in producing complex surface topography. To this end, a deviation from the reference case is needed to demonstrate several other alternative configurations that could yield different deformation modes.

5.7.1 Inclusion Geometry

Up till this point, the investigation provided has only been limited to inclusions of rectangular shapes. In this section, the prior analysis is extended to include inclusions of varying geometry. Fig.5.13 demonstrates the deformation modes for the three different cases of inclusions. The distance between the inclusion and the surface is the same for all the considered cases.

First, consider diamond shaped inclusions shown in Fig.5.13a. The buckling of the stiff matrix surrounding each inclusion follows the inclusion shape, demonstrating a narrow peaked wrinkle as shown in Fig.5.13b. The deformed surface then consists of very narrow peaks, allowing for sharp surfaces.

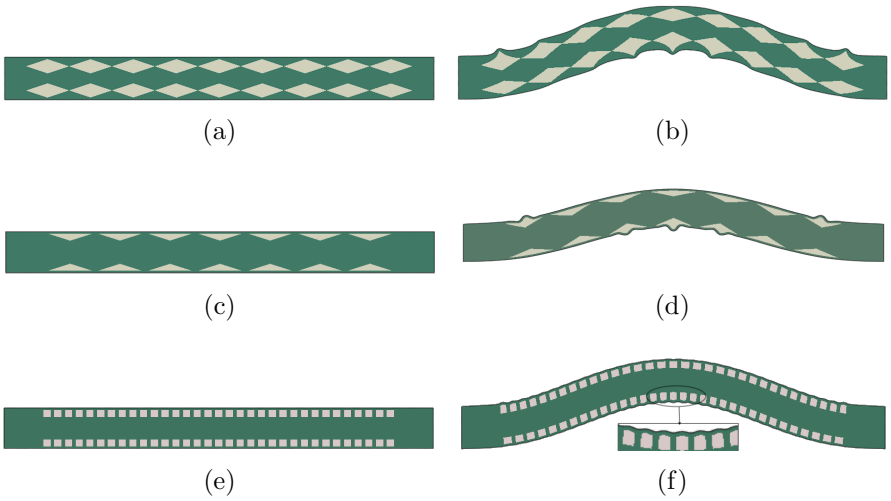

Figure 5.13: Effect of inclusion geometry on the deformation modes of the fibril with soft inclusions, (a) diamond, (c) triangular, and (e) square inclusions with (b), (d), and (f) being the respective deformed shapes.

Triangular inclusions, as shown in Fig.5.13c, result in surface wrinkles that are based on the distribution of stiffness as demonstrated in Fig.5.13d. As the stiffness underneath the rib approaches that of the matrix material, the surface displacements vanishes resulting in almost flat connections between the centers of the inclusions.

Fig.5.13f demonstrates the deformation patterns associated with small square inclusions as shown in Fig.5.13e, the small square inclusions allows for the matrix to deform in a wavy pattern. It should be noted that the stiffness of the inclusions plays a significant role in the amplitude of the wrinkles.

5.7.2 Non-uniform Arrays

The impact of arraying the inclusions has yet to be understood, in the reference case and in all subsequent analysis only two identical arrays of inclusions were considered. In this section, the impact of arraying the inclusions within the fibril is discussed. Through this analysis, the results for two different cases of arrays for square inclusions are demonstrated. For the configuration demonstrated in Fig.5.14a, the behavior is similar to that observed in Fig.5.13f, with the matrix rib having a half sine deformed shape. However, it is also observed that the stresses are more localized causing higher deformation amplitudes. For the configuration shown in Fig.5.14c, the inclusions are arrayed to allow for a softer overall section between every other inclusion. This specific distribution results in bisected peaks as shown in Fig.5.14d, because the softer sections deform more readily when compared to sections with only a single inclusion.

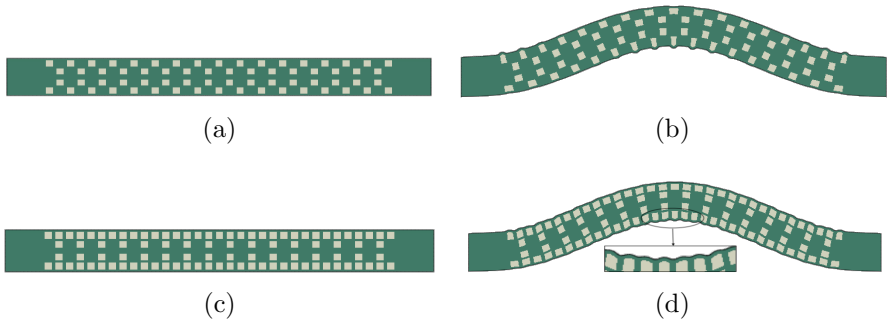

Figure 5.14: Effect of inclusion arraying on the deformation modes of the fibril with soft inclusions, (a) four arrays with square inclusions distributed in a staggered manner, and (c) four arrays with square inclusions distributed in non-staggered manner, with (b) and (d) being the respective deformed shapes.

5.7.3 Inclusion Stiffness Distribution

Previously, the impact of inclusion stiffness was discussed, however, the stiffness of the inclusion remained constant. In this section, the impact of varying substrate stiffness along the fibril thickness is considered. This was done through including another inclusion with stiffness E_e within the body of the initial substrate. Two cases are evaluated to study the different deformations. First, consider a case where the

inclusion is softened by adding another inclusion with a lower modulus of elasticity, such that $E_e < E_i$ as shown in Fig.5.15a. The addition of a second softer inclusion contributed to the emergence of channel-like deformations on the bottom surface, and a wavy upper surface as demonstrated in Fig.5.15b. This behavior is attributed

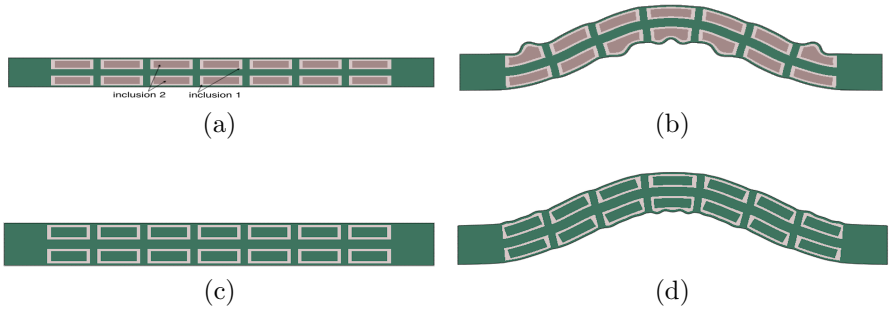

Figure 5.15: Effect of inclusion stiffness distribution on the deformation modes of the fibril with soft inclusions: (a) softer inclusions is embedded within the main inclusion, and (c) a stiffer inclusion with $E_e = E_m$ embedded within the main inclusions, with (b) and (d) being the respective deformed shapes.

to sections with inclusions experiencing significantly larger deformations than the sections without inclusions. Secondly, if the second inclusion has a similar stiffness to the matrix material ($E_e = E_m$) as seen in Fig.5.15c, a step like surface emerges. The surface morphology changes due to the stiff inclusions resisting the deformations caused by the buckling of the surface as illustrated in Fig.5.15d. Furthermore, the wrinkling of the middle inclusions is substantially altered showing variations in the peak amplitudes due to varying stiffness underneath the rib.

5.8 Fibril Aspect Ratio Larger than Rib Aspect Ratio ($t/L \gg t_r/L_i$)

So far the discussion has been particular to deformations of a fibril with a small aspect ratio, such that the local instabilities ire induced by the global buckling of the fibril. However, it is also important to consider the limit where the aspect ratio of fibril is significantly larger than that of the rib resting on the soft substrate. When $t/L \gg t_r/L_i$, local instabilities emerge without global buckling occuring. The realization of this limit implies that each section in the fibril for which an

inclusion exists will behave as a thin film resting on a multilayered substrate. Surface morphologies due to the buckling of thin films resting on elastic substrates have been investigated for layers of constant stiffness [51, 52], elastic graded substrate [53], or for fiber stiffened substrate [54]. However, to the best of our knowledge, no studies have been conducted on composite system consisting of multiple distributed soft inclusions. In composite structures, it would be possible to tune the surface morphologies based on the distribution of soft inclusions around the surface, similar to what was proposed in Sect. 5.7.

To illustrate the behavior of fibrils with aspect ratios much larger than the rib aspect ratio, a fibril with $L = 440\ \mu m$, $L_i = 30\ \mu m$, $t = 100\ \mu m$, $t_r = 3\ \mu m$, $SR = 100$, $S = 10\ \mu m$, and $c = 74\ \mu m$ is considered as shown in Fig.5.16a. Prior to global buckling, the top and bottom deformations are symmetric, thus

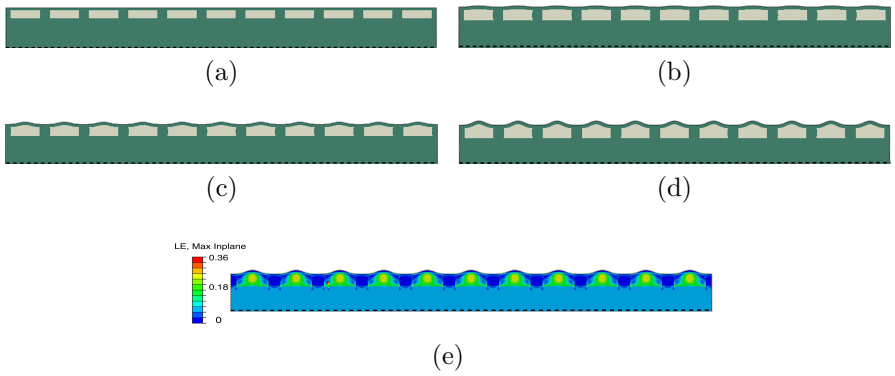

Figure 5.16: Deformation of the thick fibril with soft inclusions exhibit local buckling prior to global buckling: (a) underformed configuration, (b) deformed shape at 12 μm end shortening, (c) deformed shape at 20 μm end shortening, (d) deformed shape at 32 μm end shortening, and (e) the max in-plane strain at 32 μm end shortening.

only the top half is presented. As shown in Fig,5.16b, as the fibril undergoes end shortening of 12 μm the rib starts to bend over the elastic substrate causing the surface to start wrinkling. Fig.5.16c demonstrates the deformed surface at 20 μm end shortening with an observable increase in the peak amplitude α (the distance between the highest and the lowest points on the surface). Fig.5.16d demonstrates surface deformations prior to global buckling of the fibril. The maximum in-plane strain is shown in Fig.5.16e displaying localized strains in the elastic inclusions.

Fig.5.17 demonstrates the relationship between the peak amplitude α and the

ratio of end shortening to fibril length (u/L) prior to global buckling. The sudden growth in amplitude indicates the emergence of local instability.

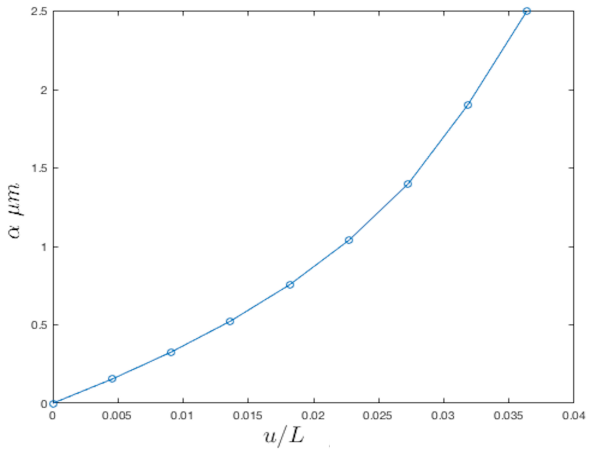

Figure 5.17: The relationship between ratio of end shortening to fibril length and the peak amplitude, demonstrating significant surface morphologies.

In Fig.5.18, it is shown that by including an additional array of soft inclusions, it is possible to substantially alter the surface morphology to include bisecting peaks, and varying peaks along the fibril length. This behavior is due to the second array of inclusions not being perfectly aligned with the one above it, allowing for a varying behavior based on the distribution of stiffness under the surface. The possible configurations for soft inclusions are numerous, allowing for tunnability and controllablity of the surface patterns. This allows a great deal of flexibility in the design process, compared to thin films resting on an elastic substrate.

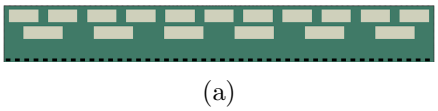

(a)

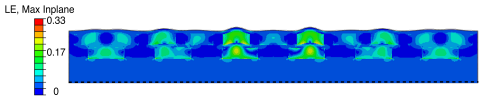

(b)

Figure 5.18: Effect of adding an additional array of inclusions: (a) the distribution of the new array of inclusions, and (b) the maximum in-plane strain localized in the inclusions showing varying surface deformations.

CHAPTER 6

DYNAMICS OF FIBRIL WITH SOFT INCLUSIONS

6.1 Natural Frequency

To determine the natural frequencies ω of the composite fibril, the generalized eigenvalue problem $[K - \omega^2 M = 0]$ is solved, where K is the stiffness matrix and M is the mass matrix. The problem setup is presented in Chapter 3; the thickness (t) and length (L_i) of the inclusion are 4 μm and 40 μm, respectively, and the stiffness ratio is $E_m/E_i = 100$. The tangent stiffness matrix and the mass matrix are obtained form the finite element formulation and a Lancoz algorithm is utilized to solve the generalized eigenvalue problem.

In this chapter, 4 different cases are evaluated, where the fibril buckles globally under 12 μm end shortening. First, a reference buckled homogeneous fibril is considered, for which the first three eigenmodes and corresponding frequencies ω^2 are shown in Fig.6.2. It is observable that for a homogeneous fibril in the post-buckled configuration, ω^2 associated with the first mode remains positive as illustrated in Fig.6.2a. The positive ω^2 indicates positive post-buckling stiffness. A similar analysis is conducted on a fibril with a single soft inclusion, where a distinguishable observation is made from the reference case. In fibrils with soft inclusions localized modes emerge due to localized deformation. Prior to local instability the associated ω^2 with the first localized mode is positive, however, post local instability the ω^2 for this mode becomes negative as illustrated in Fig.6.1d; this is indicative of unstable local instability. In Fig.6.5 the relationship between the ratio of end shortening to the total fibril length versus ω^2 is shown to demonstrate the transition of the local mode from positive to a negative ω^2 due to local instability.

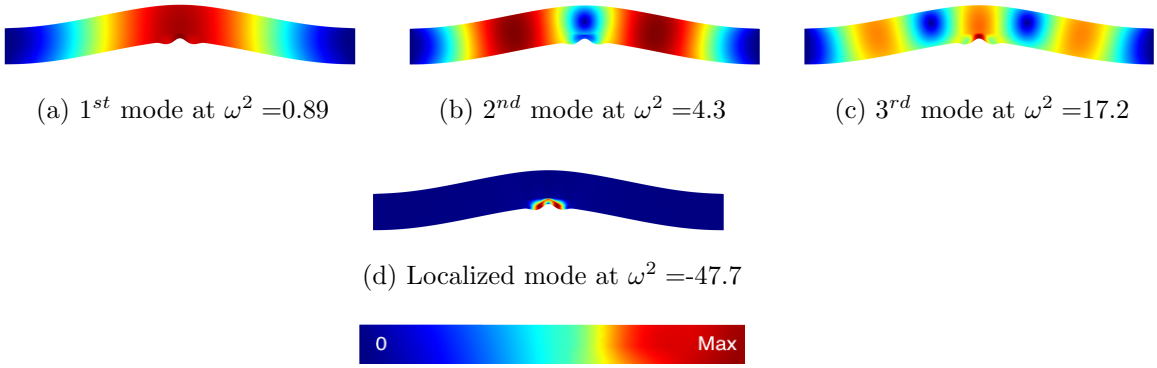

(a) 1^{st} mode at ω^2 =0.89 (b) 2^{nd} mode at ω^2 =4.3 (c) 3^{rd} mode at ω^2 =17.2

(d) Localized mode at ω^2 =-47.7

Figure 6.1: Frequency ω^2 in $\text{rad}^2\text{s}^{-2} \times 10^{12}$ and associated eigen modes for a fibril with a single inclusion, showing the first three modes (a,b,c) and localized mode (d)

The analysis is then expanded to two other cases: (1) a fibril with multiple patterned soft inclusions which exhibits negative post-buckling stiffness, and (2) a fibril with multiple patterned voids with positive post-buckling stiffness. Both cases observe local instabilities: however, one major difference is that in the fibril with soft inclusions the local bifurcation behavior is unstable. It is demonstrated in Fig.6.3d that the first local mode of instability has negative ω^2. The transition from positive ω^2 to negative is illustrated in Fig.6.5 for a fibril with multiple patterned soft inclusions. While in the case of voided fibril, the first localized mode remains positive as shown in Fig.6.4d.

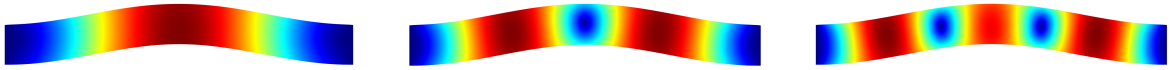

(a) 1^{st} mode at ω^2 =0.48 (b) 2^{nd} mode at ω^2 =3.8 (c) 3^{rd} mode at ω^2 =18.25

Figure 6.2: Frequency ω^2 in $\text{rad}^2\text{s}^{-2} \times 10^{12}$ and associated eigen modes for a homogeneous fibril, showing the first three modes(a,b,c).

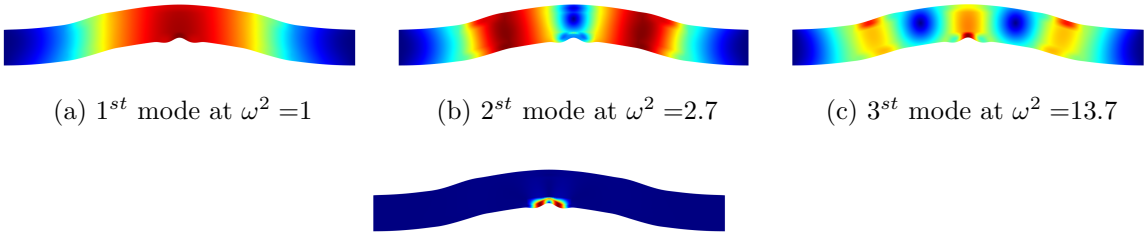

(a) 1^{st} mode at ω^2 =1 (b) 2^{st} mode at ω^2 =2.7 (c) 3^{st} mode at ω^2 =13.7

(d) localized mode at ω^2 =-29.9

Figure 6.3: Frequency ω^2 in $\text{rad}^2\text{s}^{-2} \times 10^{12}$ and associated eigen modes for a fibril with patterned inclusions, showing the first three modes (a,b,c) and localized mode (d).

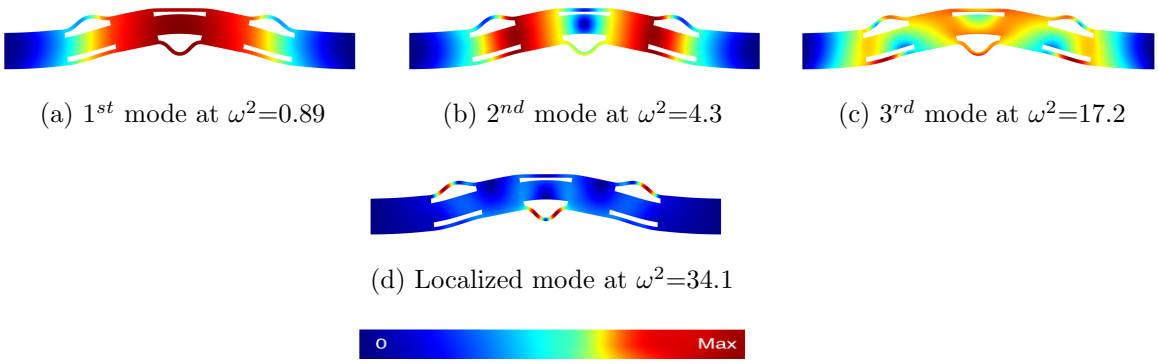

(a) 1^{st} mode at ω^2=0.89 (b) 2^{nd} mode at ω^2=4.3 (c) 3^{rd} mode at ω^2=17.2

(d) Localized mode at ω^2=34.1

Figure 6.4: Frequency ω^2 in $\text{rad}^2\text{s}^{-2} \times 10^{12}$ and associated eigen modes for a fibril with patterned voids, showing the first three modes (a,b,c) and localized mode (d).

6.2 Band Gap Analysis

Mechanically triggered large deformation, instability-induced interfacial wrinkling, and tension-induced tunable corrugations have been harnessed to tune the evolution of elastic and acoustic band gaps [7, 11, 55, 56]. Bragg diffraction and local resonance are the two mechanisms that govern the band gap emergence in composite materials [57, 58]. Bragg diffraction is observed when both the elastic wavelength and the periodicity of the structure are similar. This band-gap profile can be tuned by material design [59, 60, 61], and controlled deformations pattern [62]. Local res-

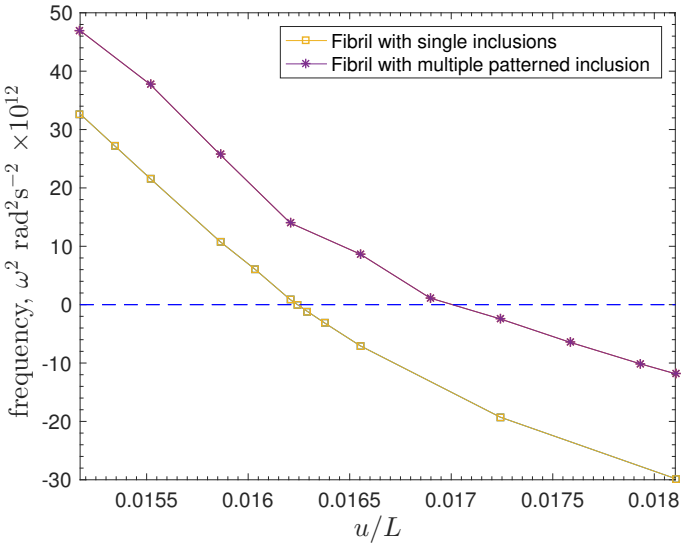

Figure 6.5: The relationship between ratio of end shortening to fibril length and ω^2 for the localized mode, demonstrating the transition from positive to negative due to instability

onance is a direct consequence of the contrast between phases within the composite structure.

In this section we focus on investigating the influence of negative post-buckling stiffness on the band gap structure of the composite fibril with soft inclusion. For that purpose, Bloch wave analysis is conducted to evaluate the emergence and evolution of band-gaps for buckled fibrils with soft inclusions, using the procedure described in Chapter 3. We also consider, for comparison purposes, the band-gap structure for a fibril with single void. For the soft inclusion case, two sub-cases are considered: (1) a single inclusion, and (2) multiple distributed inclusions. The geometry and material properties is the same as those presented in Section 3; the thickness (t) and length(L_i) of the inclusion are 4 μm and 40 μm, respectively, and the stiffness ratio is $E_m/E_i = 100$. Bloch wave boundary conditions is applied as mentioned in Sect. 2.3.

First, let us consider the band gap evolution profile for a fibril with a single inclusions as shown in Fig.6.6a. It is shown that buckled fibrils with soft inclusions demonstrate widening band-gaps in the lower frequency range. Five narrow band gaps are initially observed at 9 μm end shortening within [0.48, 0.55], [0.85, 0.86],

[0.90, 0.905], [1.20, 1.25], and [1.759, 1.768] MHz. It is also demonstrated that with further end shortening, most of the band gaps observed widen. At 17 μm end shortening, four of the five band-gaps initially observed expand within [0.39, 0.65], [0.72, 0.85], [0.96, 1.03], and [1.15, 1.30] MHz. This observation indicates the significant contribution end shortening has on the band-gap structure of composite fibrils.

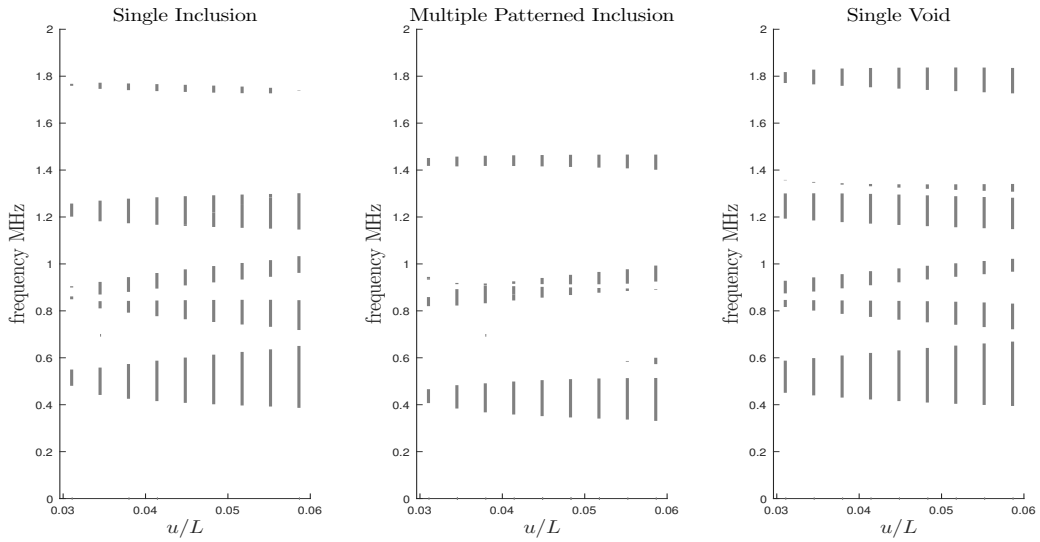

Figure 6.6: The band gap structure evolution for fibrils with soft inclusions demonstrating widening band gaps with increased loading, (a) fibril with single inclusion in its buckled configuration, (b) fibril with multiple inclusions in its buckled configuration, and (c) fibril with single void in its buckled configuration.

To evaluate the impact of multiple inclusions within the fibril, the results for the band gap evolution is illustrated in Fig.6.6b. It is observed that at 9 μm end shortening, three narrow band gaps emerge within [0.40, 0.47], [0.82, 0.86] and [1.41, 1.45] MHz. Similar observations are made showing that as the fibril undergoes deformation, these band gaps widen to [0.33, 0.51], [0.92, 1], and [1.4, 1.46] MHz. An emergence of additional low frequency band gap is observed at 17μm end shortening within [0.57-0.60] MHz. We note two distinguishable differences between these two cases. Due to the addition of inclusions, the stiffness of the fibril is reduced contributing to lower band gap frequencies. Furthermore, incorporating inclusions

altered the overall band-gap structure of the fibril such that fewer gaps are observed.

The existence of band gaps in porous structures is well documented in the literature [63, 64], thus, it is interesting to study whether a fibril with soft inclusions can produce comparable band gaps as a fibril with voids. The band gap evolution of a fibril with single void is shown in Fig.6.6c. Initially, at $9\mu m$ end shortening, the fibril with voids shows three wider band-gaps than observed in the fibril with single inclusion within [0.45, 0.59], [0.87, 0.93], and [1.77, 1.82] MHz. However, with further loading, the response of both cases converge to similar band gaps with the exception of a high frequency band gap within [1.73, 1.84] MHz.

It is noted that a homogeneous fibril has no band gaps before or after buckling, and that through adding a single soft inclusion, the band gap structure for the fibril is completely altered.

CHAPTER 7

DISCUSSION

We aim to shed some light on the interesting features of composite materials with soft inclusions. To this end, we study the behavior of a two-phase composite fibril made of a stiff matrix and soft inclusions under large compressive deformations. It is demonstrated that fibrils with soft inclusions have negative post-buckling stiffness. We further showed that local instabilities contribute to the emergence of surface morphologies associated with the buckling modes. Dynamics of the fibril are also studied to demonstrate how the soft inclusion alters the natural frequencies of the system, and show the emergence, and evolution of band-gaps using Bloch wave analysis.

Discontinuous buckling describes a system that exhibits negative post-buckling stiffness. While this behavior is observed in complex systems [65], and in some meta-materials [30], the utilization of soft inclusion to induce such response has not been mentioned. Through a finite element model, it was demonstrated that a composite fibril with soft inclusion can exhibit unstable post-buckling response, where the axial stiffness of the fibril becomes negative. This behavior is attributed to the local instabilities induced by the global buckling of the fibril. As the fibril buckles globally, stress is concentrated in the vicinity of the inclusion causing the stiff matrix surrounding the inclusion to buckle on the soft substrate underneath. This local behavior contributes to the transition from positive stiffness to negative stiffness.

To further explain the unstable behavior of the local instability, we postulated that the global buckling causes bending moments around the rib resting on an elastic foundation, that in turn causes the rib to buckle. We isolated this specific behavior and developed a semi-analytical approach to solve the non-linear problem of a beam resting on an elastic foundation. Through minimizing the strain energy functional V, it is demonstrated in Fig.4.5 that the rib does experience unstable

post-buckling response for any perturbed amplitude. The analysis is expanded to evaluate the response of changing foundation modulus, mimicking a change in inclusion thickness or stiffness. It was observed in Fig.4.6 that the post-buckling response varies significantly with the substrate modulus showing a non-monotonic behavior. The negative normalized stiffness of the fibril vanishes in the limit $k \to 0$, while in the case of SR=1 ($E_i = E_m$) local buckling does not manifest. These results validate the numerical results produced in Chapter 5.

We note that while the semi-analytical model captures the unstable post-buckling response of the beam resting on a substrate, there are several limitations to the current model.

- The model assumes that the normalized end moments are symmetric, while during the global buckling of fibrils that is not entirely the case, similar to the observations made in the multiple inclusion case.

- The model does not capture the nonlinearities of the elastic substrate.

The deformation modes that couple the global and local behavior produce rich surface morphologies, such as wrinkles and folds. Similar surface morphologies have been recently associated with enhanced mechanical, and acoustic properties with applications in tunnable adhesion [66], diffraction grading [67], and electronic devices [68]. Furthermore, recent interest has been seen toward the manufacturing of deployable 2D structures that can transform into 3D structures using compressive buckling [69, 70]. The fibril presented in this study can be utilized in similar applications, and further tuned to obtain edges using thicker inclusions as shown in Fig.5.5, or wavy surfaces using longer inclusions as shown in Fig.5.8.

Through the simulations, it was shown that both the post-buckling stiffness and the surface morphologies can be controlled through inclusions patterning, dimensions, and stiffness. We observed that although a single inclusion, as shown in Fig.2.1a, is capable of producing unstable post-buckling response, the negative stiffness is enhanced through the distribution of inclusions within the matrix material as observed in Fig. 5.1b. It is shown both numerically and analytically that the post-buckling response does not behave monotonically with the change in the inclusion stiffness.

Several other modifications to the fibril were considered to uncover the impact of other parameters on the surface topography, as discussed in Sect.5.7. Through

different choices of inclusion geometry, as shown in Fig.5.13, the surface topography of the post buckled beam varied substantially. Non-uniform arrays of inclusions further altered the surface topology through inclusion interacting between each array as shown in Fig.5.14. Additional consideration was given to the stiffness distribution within the fibril. It was demonstrated in Fig.5.15 that surface morphologies vary significantly according to the distribution of stiffness in the fibril.

Studies on the buckling of thin films attached to elastic substrate demonstrated the capabilities of producing surface morphologies such as wrinkles, creases and folds. However, this bilayered system lacks the flexibility to produce varying surface topography. To demonstrate the potential of fibrils with soft inclusions in producing tunnable surfaces without global buckling, the case of fibril aspect ratio exceeding that of rib resting on the elastic substrate was considered. As illustrated in Fig.5.16, the local instabilities emerge prior to the global buckling, resulting in surface wrinkles with amplitude that varies based on end shortening ratio to fibril length. Furthermore, it was shown in Fig.5.18 that through modifying inclusions' distribution within the fibril, the surface topology could change along the length of the fibril to form bisecting peaks or peaks with different amplitudes.

A natural frequency analysis was conducted to study the dynamic response of buckled fibril composites with soft inclusions. The behavior of fibril with soft inclusions was compared to a reference homogeneous case. For a fibril with soft inclusions post the local instability behavior, it was demonstrated that localized modes with negative ω^2 emerge; such behavior is absent in the case of a homogeneous fibril. The cases of multiple patterned inclusions and voids were also considered. It was observed that negative ω^2 was specific to the fibril with soft inclusions due to the negative post-buckling stiffness. The negative frequencies are a direct consequence of the unstable post-buckling response. The localized modes with negative ω^2 correspond to linearly unstable modes.

Bloch wave analysis was conducted on the buckled fibrils to evaluate the wave propagation properties of the fibrils with soft inclusions. It was observed that post buckling fibrils with soft inclusions have stop band that bar the propagation of elastic waves in the structure. These band-gaps emerge due to the local resonance effect in the vicinity of the inclusion. It was shown in Fig.6.6a that the fibril with soft inclusion has a low frequency band-gap, while fibrils with multiple patterned inclusions demonstrated less band-gaps. The behavior of the fibril with a single

inclusion remains similar in the limit of the inclusion stiffness going to zero (void), however, an emergence of high frequency bands for the void case was observed. For all three cases the band-gaps widen as the system is progressively loaded, indicating possible modulation of band-gaps through controlled loading.

We note that in the above analysis, perfect bonding between the inclusion and the matrix was assumed. While the possibility of cavitation on the tension side of the substrate due to the debonding between the matrix and inclusion does exist, cavitations could be limited by surface treatments. In our analysis, the stresses, and strains are within the material limits. Accordingly, this process is entirely reversible, and through unloading the original undeformed configuration of the fibril can be retrieved. This opens pathways for modulating and tuning the dynamic response of the fibril based on specific needs.

Through this study, we aimed to propose different elements to the current material design paradigm offering interesting mechanical features, such as discontinuous buckling and surface morphologies. We expect that the negative post buckling stiffness could be utilized in developing negative stiffness systems with applications in vibration isolation [71], damping [72], and enhanced energy harvesting[73]. We hope that surface morphologies of fibrils with soft inclusions can be utilized in assemblage of complex systems [74], photonic switching [75], or other applications. Finally, we note the possibility of incorporating topology optimization in identifying the ideal inclusions' patterning for any specific application, whether it is vibration damping, surface morphologies, or tuning band-gap structure.

REFERENCES

[1] R. D. Farahani, M. Dubé, and D. Therriault, "Three-Dimensional Printing of Multifunctional Nanocomposites: Manufacturing Techniques and Applications," *Advanced Materials*, pp. 5794–5821, 2016.

[2] Q. Chen and A. Elbanna, "Tension-induced tunable corrugation in two-phase soft composites: Mechanisms and implications," *Extreme Mechanics Letters*, vol. 4, pp. 26–37, 2015. [Online]. Available: http://dx.doi.org/10.1016/j.eml.2015.07.009

[3] J. Yin, J. L. Yagüe, M. C. Boyce, and K. K. Gleason, "Biaxially mechanical tuning of 2-D reversible and irreversible surface topologies through simultaneous and sequential wrinkling," *ACS Applied Materials and Interfaces*, vol. 6, no. 4, pp. 2850–2857, 2014.

[4] W. K. Lee, C. J. Engel, M. D. Huntington, J. Hu, and T. W. Odom, "Controlled Three-Dimensional Hierarchical Structuring by Memory-Based, Sequential Wrinkling," *Nano Letters*, vol. 15, no. 8, pp. 5624–5629, 2015.

[5] J. L. Silverberg, A. A. Evans, L. McLeod, R. C. Hayward, T. Hull, C. D. Santangelo, and I. Cohen, "Using origami design principles to fold reprogrammable mechanical metamaterials," *Science*, vol. 345, no. 6197, pp. 647–650, 2014. [Online]. Available: http://www.sciencemag.org/cgi/doi/10.1126/science.1252876

[6] S. Yang, K. Khare, and P. C. Lin, "Harnessing surface wrinkle patterns in soft matter," *Advanced Functional Materials*, vol. 20, no. 16, pp. 2550–2564, 2010.

[7] Q. Chen and A. Elbanna, "Modulating Elastic Band Gap Structure in Layered Soft Composites Using Sacrificial Interfaces," *Journal of Applied Mechanics*, vol. 83, no. 11, p. 111009, 2016.

[8] C. M. Chen and S. Yang, "Wrinkling instabilities in polymer films and their applications," *Polymer International*, vol. 61, no. 7, pp. 1041–1047, 2012.

[9] M. Guttag and M. C. Boyce, "Locally and dynamically controllable surface topography through the use of particle-enhanced soft composites," *Advanced Functional Materials*, vol. 25, no. 24, pp. 3641–3647, 2015.

[10] F. Javid, J. Liu, J. Shim, J. C. Weaver, A. Shanian, and K. Bertoldi, "Mechanics of instability-induced pattern transformations in elastomeric porous cylinders," *Journal of the Mechanics and Physics of Solids*, vol. 96, pp. 1–17, 2016. [Online]. Available: http://dx.doi.org/10.1016/j.jmps.2016.06.015

[11] K. Bertoldi, M. C. Boyce, S. Deschanel, S. M. Prange, and T. Mullin, "Mechanics of deformation-triggered pattern transformations and superelastic behavior in periodic elastomeric structures," *Journal of the Mechanics and Physics of Solids*, vol. 56, no. 8, pp. 2642–2668, 2008.

[12] G. Wu, Y. Xia, and S. Yang, "Buckling, symmetry breaking, and cavitation in periodically micro-structured hydrogel membranes," *Soft Matter*, vol. 10, no. 9, pp. 1392–1399, 2014. [Online]. Available: http://xlink.rsc.org/?DOI=C3SM51640G

[13] R. W. Style, R. Boltyanskiy, B. Allen, K. E. Jensen, H. P. Foote, J. S. Wettlaufer, and E. R. Dufresne, "Stiffening solids with liquid inclusions," vol. 11, no. December 2014, 2014. [Online]. Available: http://arxiv.org/abs/1407.6424%0Ahttp://dx.doi.org/10.1038/nphys3181

[14] G. Falzone, G. P. Falla, Z. Wei, M. Zhao, A. Kumar, M. Bauchy, N. Neithalath, L. Pilon, and G. Sant, "The influences of soft and stiff inclusions on the mechanical properties of cementitious composites," *Cement and Concrete Composites*, vol. 71, pp. 153–165, 2016. [Online]. Available: http://dx.doi.org/10.1016/j.cemconcomp.2016.05.008

[15] S. Pilehvar, V. D. Cao, A. M. Szczotok, L. Valentini, D. Salvioni, M. Magistri, R. Pamies, and A. L. Kjøniksen, "Mechanical properties and microscale changes of geopolymer concrete and Portland cement concrete containing micro-encapsulated phase change materials," *Cement and Concrete Research*, vol. 100, no. February, pp. 341–349, 2017. [Online]. Available: http://dx.doi.org/10.1016/j.cemconres.2017.07.012

[16] M. Diab, T. Zhang, R. Zhao, H. Gao, and K.-S. Kim, "Ruga mechanics of creasing: from instantaneous to setback creases," *Proceedings of the Royal Society A: Mathematical, Physical and Engineering Sciences*, vol. 469, no. 2157, pp. 20 120 753–20 120 753, 2013. [Online]. Available: http://rspa.royalsocietypublishing.org/content/469/2157/20120753

[17] A. Goriely, M. G. Geers, G. A. Holzapfel, J. Jayamohan, A. Jérusalem, S. Sivaloganathan, W. Squier, J. A. van Dommelen, S. Waters, and E. Kuhl, "Mechanics of the brain: perspectives, challenges, and opportunities," *Biomechanics and Modeling in Mechanobiology*, vol. 14, no. 5, pp. 931–965, 2015. [Online]. Available: http://dx.doi.org/10.1007/s10237-015-0662-4

[18] X. Chen and J. Yin, "Buckling patterns of thin films on curved compliant substrates with applications to morphogenesis and three-dimensional microfabrication," *Soft Matter*, vol. 6, no. 22, p. 5667, 2010. [Online]. Available: http://xlink.rsc.org/?DOI=c0sm00401d

[19] Z. G. Nicolaou and A. E. Motter, "Mechanical metamaterials with negative compressibility transitions," *Nature Materials*, vol. 11, no. 7, pp. 608–613, 2012. [Online]. Available: http://www.nature.com/doifinder/10.1038/nmat3331

[20] B. A. Fulcher, D. W. Shahan, M. R. Haberman, C. Conner Seepersad, and P. S. Wilson, "Analytical and Experimental Investigation of Buckled Beams as Negative Stiffness Elements for Passive Vibration and Shock Isolation Systems," *Journal of Vibration and Acoustics*, vol. 136, no. 3, p. 031009, 2014.

[21] J. T. B. Overvelde, T. Kloek, J. J. A. D'haen, and K. Bertoldi, "Amplifying the response of soft actuators by harnessing snap-through instabilities," *Proceedings of the National Academy of Sciences*, vol. 112, no. 35, pp. 10 863–10 868, 2015. [Online]. Available: http://www.pnas.org/lookup/doi/10.1073/pnas.1504947112

[22] S. Xu, Z. Yan, K.-I. Jang, W. Huang, H. Fu, J. Kim, Z. Wei, M. Flavin, J. McCracken, R. Wang, A. Badea, Y. Liu, D. Xiao, G. Zhou, J. Lee, H. U. Chung, H. Cheng, W. Ren, A. Banks, X. Li, U. Paik, R. G. Nuzzo, Y. Huang, Y. Zhang, and J. A. Rogers, "Assembly of micro/nanomaterials into complex, three-dimensional architectures by compressive buckling," *Science*, vol. 347, no. 6218, pp. 154–159, 2015. [Online]. Available: http://www.sciencemag.org/cgi/doi/10.1126/science.1260960

[23] D. M. Correa, T. Klatt, S. Cortes, M. Haberman, D. Kovar, and C. Seepersad, "Negative stiffness honeycombs for recoverable shock isolation," *Rapid Prototyping Journal*, vol. 21, no. 2, pp. 193–200, 2015. [Online]. Available: http://www.emeraldinsight.com/doi/abs/10.1108/RPJ-12-2014-0182

[24] S. Cortes, J. Allison, C. Morris, M. R. Haberman, C. C. Seepersad, and D. Kovar, "Design, Manufacture, and Quasi-Static Testing of Metallic Negative Stiffness Structures within a Polymer Matrix," *Experimental Mechanics*, pp. 1–9, 2017.

[25] C. Keplinger, T. Li, R. Baumgartner, Z. Suo, and S. Bauer, "Harnessing snap-through instability in soft dielectrics to achieve giant voltage-triggered deformation," *Soft Matter*, vol. 8, no. 2, pp. 285–288, 2012. [Online]. Available: http://xlink.rsc.org/?DOI=C1SM06736B

[26] A. A. Zadpoor, "Mechanical meta-materials," *Mater. Horiz.*, vol. 3, no. 5, pp. 371–381, 2016. [Online]. Available: http://xlink.rsc.org/?DOI=C6MH00065G

[27] J. Zhu, M. Dexheimer, and H. Cheng, "Reconfigurable systems for multifunctional electronics," *npj Flexible Electronics*, vol. 1, no. 1, p. 8, 2017. [Online]. Available: http://www.nature.com/articles/s41528-017-0009-6

[28] S. Goldstein, J. Campbell, and T. Mowry, "Programmable matter," *Computer*, vol. 38, no. 6, pp. 99–101, 2005. [Online]. Available: http://ieeexplore.ieee.org/document/1439465/

[29] S. Singamaneni, K. Bertoldi, S. Chang, J. H. Jang, E. L. Thomas, M. C. Boyce, and V. V. Tsukruk, "Instabilities and pattern transformation in periodic, porous elastoplastic solid coatings," *ACS Applied Materials and Interfaces*, vol. 1, no. 1, pp. 42–47, 2009.

[30] C. Coulais, J. T. B. Overvelde, L. A. Lubbers, K. Bertoldi, and M. Van Hecke, "Discontinuous Buckling of Wide Beams and Metabeams," *Physical Review Letters*, vol. 115, no. 4, pp. 1–7, 2015.

[31] T. Klatt, M. Haberman, and C. C. Seepersad, "Selective laser sintering of negative stiffness mesostructures for recoverable, nearly-ideal shock isolation," *24th International SFF Symposium - An Additive Manufacturing Conference, SFF 2013*, pp. 1010–1022, 2013. [Online]. Available: http://www.scopus.com/inward/record.url?eid=2-s2.0-84898480140&partnerID=40&md5=692e6c5bd6720ec2b0ba5062270080ac

[32] H. Gao, "Application of fracture mechanics concepts to hierarchical biomechanics of bone and bone-like materials," *International Journal of Fracture*, vol. 138, no. 1-4, pp. 101–137, 2006.

[33] M. Wadee and G. Hunt, "Interactively induced localized buckling in sandwich structures with core orthotropy," *Journal of Applied Mechanics, Transactions ASME*, vol. 65, no. 2, pp. 523–528, 1998.

[34] L. Euler, "Additamentum I de curvis elasticis, methodus inveniendi lineas curvas maximi minimivi proprietate gaudentes," *Opera Omnia*, pp. 245–310, 1744.

[35] S. P. Timoshenko, "LXVI. On the correction for shear of the differential equation for transverse vibrations of prismatic bars," *Philosophical Magazine Series 6*, vol. 41, no. 245, pp. 744–746, 1921.

[36] J. Qiu, J. H. Lang, and A. H. Slocum, "A curved-beam bistable mechanism," *Journal of Microelectromechanical Systems*, vol. 13, no. 2, pp. 137–146, 2004.

[37] J. Genzer and J. Groenewold, "Soft matter with hard skin: From skin wrinkles to templating and material characterization," *Soft Matter*, vol. 2, no. 4, p. 310, 2006. [Online]. Available: http://xlink.rsc.org/?DOI=b516741h

[38] H. G. H. G. Allen, "Analysis and design of structural sandwich panels," p. 283, 1969.

[39] M. H. Huang and D. P. Thambiratnam, "Analysis of plate resting on elastic supports and elastic foundation by finite strip method," *Computers and Structures*, vol. 79, no. 29-30, pp. 2547–2557, 2001.

[40] Z. Y. Huang, W. Hong, and Z. Suo, "Nonlinear analyses of wrinkles in a film bonded to a compliant substrate," *Journal of the Mechanics and Physics of Solids*, vol. 53, no. 9, pp. 2101–2118, 2005.

[41] L. R. G. Treloar, *The Physics of Rubber Elasticity*, third edit ed. New York: Oxford University Press, 1975.

[42] M. A. Guttag, B. S. M. Engineering, M. C. Boyce, D. E. Hardt, and E. Ralph, "Tunable Surface Topographies via Particle- Enhanced Soft Composites Signature redacted Signature redacted Signature redacted," Ph.D. dissertation, Massachusetts Institute of Technology, 2015.

[43] L. Brillouin, *Wave Propagation in Periodic Structures*. Dover Publications Inc.;2nd ed. edition, 1946.

[44] M. Åberg and P. Gudmundson, "The usage of standard finite element codes for computation of dispersion relations in materials with periodic microstructure," *The Journal of the Acoustical Society of America*, vol. 102, no. 4, pp. 2007–2013, 1997. [Online]. Available: http://asa.scitation.org/doi/10.1121/1.419652

[45] J. A. Van Der Rijt, K. O. Van Der Werf, M. L. Bennink, P. J. Dijkstra, and J. Feijen, "Micromechanical testing of individual collagen fibrils," *Macromolecular Bioscience*, vol. 6, no. 9, pp. 699–702, 2006.

[46] ABAQUS, "ABAQUS Documentation," Providence, RI, USA., 2011.

[47] J. M. T. Thompson and G. W. Hunt, *A General Theory of Elastic Stability*, ser. Wiley-Interscience publication. J. Wiley, 1973. [Online]. Available: https://books.google.com/books?id=j6YeAQAAIAAJ

[48] A. M. A. van der Heijden, *W. T. Koiter's Elastic Stability of Solids and Structures*. Cambridge University Press, 2008. [Online]. Available: https://books.google.com/books?id=URcgngEACAAJ

[49] W. Koiter, "On The Stability of Elastic Equilibrium," Ph.D. dissertation, 1945.

[50] K. L. McCance, S. E. Huether, and F. Geneser, "Collagen Structure and Stability," *PLoS ONE*, vol. 78, no. 3, pp. 929–958, 2010.

[51] Y. Cao and J. W. Hutchinson, "Wrinkling Phenomena in Neo-Hookean Film/Substrate Bilayers," *Journal of Applied Mechanics*, vol. 79, no. 3, p. 031019, 2012.

[52] A. Auguste, L. Jin, Z. Suo, and R. C. Hayward, "Post-wrinkle bifurcations in elastic bilayers with modest contrast in modulus," *Extreme Mechanics Letters*, vol. 11, pp. 30–36, 2017. [Online]. Available: http://dx.doi.org/10.1016/j.eml.2016.11.013

[53] Y. P. Cao, F. Jia, Y. Zhao, X. Q. Feng, and S. W. Yu, "Buckling and post-buckling of a stiff film resting on an elastic graded substrate," *International Journal of Solids and Structures*, vol. 49, no. 13, pp. 1656–1664, 2012. [Online]. Available: http://dx.doi.org/10.1016/j.ijsolstr.2012.03.004

[54] Y. Zheng, G. Y. Li, Y. Cao, and X. Q. Feng, "Wrinkling of a stiff film resting on a fiber-filled soft substrate and its potential application as tunable metamaterials," *Extreme Mechanics Letters*, vol. 11, pp. 121–127, 2017. [Online]. Available: http://dx.doi.org/10.1016/j.eml.2016.12.002

[55] S. Rudykh and M. C. Boyce, "Transforming wave propagation in layered media via instability-induced interfacial wrinkling," *Physical Review Letters*, vol. 112, no. 3, pp. 1–5, 2014.

[56] K. Bertoldi and M. C. Boyce, "Wave propagation and instabilities in monolithic and periodically structured elastomeric materials undergoing large deformations," *Physical Review B - Condensed Matter and Materials Physics*, vol. 78, no. 18, pp. 1–16, 2008.

[57] C. Goffaux and J. Sánchez-Dehesa, "Two-dimensional phononic crystals studied using a variational method: Application to lattices of locally resonant materials," *Physical Review B*, vol. 67, no. 14, p. 144301, 2003. [Online]. Available: https://link.aps.org/doi/10.1103/PhysRevB.67.144301

[58] Y. Achaoui, A. Khelif, S. Benchabane, L. Robert, and V. Laude, "Experimental observation of locally-resonant and Bragg band gaps for surface guided waves in a phononic crystal of pillars," *Physical Review B - Condensed Matter and Materials Physics*, vol. 83, no. 10, pp. 1–5, 2011.

[59] C. Goffaux and J. P. Vigneron, "Theoretical study of a tunable phononic band gap system," *Physical Review B*, vol. 64, no. 7, p. 075118, 2001. [Online]. Available: https://link.aps.org/doi/10.1103/PhysRevB.64.075118

[60] O. Sigmund and J. Søndergaard Jensen, "Systematic design of phononic band-gap materials and structures by topology optimization," *Philosophical Transactions of the Royal Society of London A: Mathematical, Physical and Engineering Sciences*, vol. 361, no. 1806, pp. 1001–1019, 2003. [Online]. Available: http://rsta.royalsocietypublishing.org/content/361/1806/1001

[61] S. L. Vatanabe, G. H. Paulino, and E. C. N. Silva, "Maximizing phononic band gaps in piezocomposite materials by means of topology optimization," *The Journal of the Acoustical Society of America*, vol. 136, no. 2, pp. 494–501, 2014. [Online]. Available: http://asa.scitation.org/doi/10.1121/1.4887456

[62] A. Bayat and F. Gordaninejad, "Switching band-gaps of a phononic crystal slab by surface instability," *Smart Materials and Structures*, vol. 24, no. 7, p. 075009, 2015. [Online]. Available: http://stacks.iop.org/0964-1726/24/i=7/a=075009?key=crossref.61a7fe24c542ea8645eec3285cb698df

[63] M. J. Leamy and J. H. Nadler, "Acoustic Band-Gap Formulation in Infinite Periodic Porous Media With a Multi-Layered Unit Cell: Multi-Scale Asymptotic Method," pp. 1–9, 2017.

[64] J. O. Vasseur, P. A. Deymier, G. Frantziskonis, G. Hong, B. Djafari-Rouhani, and L. Dobrzynski, "periodic composite media Experimental evidence for the existence of absolute acoustic band gaps in two-dimensional periodic composite media," *Journal of Physics: Condensed Matter*, vol. 6051, 1998.

[65] T. Mizuno, T. Toumiya, and M. Takasaki, "Vibration isolation system using negative stiffness," pp. 807–812, 2003. [Online]. Available: http://jlc.jst.go.jp/JST.JSTAGE/jsmec/46.807?from=Google

[66] E. P. Chan, E. J. Smith, R. C. Hayward, and A. J. Crosby, "Surface wrinkles for smart adhesion," *Advanced Materials*, vol. 20, no. 4, pp. 711–716, 2008.

[67] C. Harrison, C. M. Stafford, W. Zhang, A. Karim, C. Harrison, C. M. Stafford, W. Zhang, and A. Karim, "Sinusoidal phase grating created by a tunably buckled surface," *Applied Physics Letters*, vol. 4016, no. 2004, 2010.

[68] D.-Y. Khang, H. Jiang, Y. Huang, and J. A. Rogers, "A Stretchable Form of Single-Crystal," *Science*, vol. 311, no. January, pp. 208–212, 2006.

[69] X. Ning, H. Wang, X. Yu, J. A. Soares, Z. Yan, K. Nan, G. Velarde, Y. Xue, R. Sun, Q. Dong, H. Luan, C. M. Lee, A. Chempakasseril, M. Han, Y. Wang, L. Li, Y. Huang, Y. Zhang, and J. A. Rogers, "3D Tunable, Multiscale, and Multistable Vibrational Micro-Platforms Assembled by Compressive Buckling," *Advanced Functional Materials*, vol. 27, no. 14, pp. 1–9, 2017.

[70] J. A. Rogers, T. Someya, and Y. Huang, "Materials and Mechanics for Stretchable Electronics," *Science*, vol. 327, no. 5973, pp. 1603–1607, 2010. [Online]. Available: http://www.sciencemag.org/cgi/doi/10.1126/science.1182383

[71] D. L. Platus, "Negative-stiffness-mechanism vibration isolation systems," *Proc. SPIE 1619, Vibration Control in Microelectronics, Optics, and Metrology*, no. February 1992, pp. 44–54, 1992. [Online]. Available: http://proceedings.spiedigitallibrary.org/proceeding.aspx?articleid=982230

[72] L. Dong and R. S. Lakes, "Advanced damper with negative structural stiffness elements," *Smart Materials and Structures*, vol. 21, no. 7, 2012.

[73] R. L. Harne, M. Thota, and K. W. Wang, "Bistable energy harvesting enhancement with an auxiliary linear oscillator," *Smart Materials and Structures*, vol. 22, no. 12, 2013.

[74] Z. Yan, F. Zhang, J. Wang, F. Liu, X. Guo, K. Nan, Q. Lin, M. Gao, D. Xiao, Y. Shi, Y. Qiu, H. Luan, J. H. Kim, Y. Wang, H. Luo, M. Han, Y. Huang, Y. Zhang, and J. A. Rogers, "Controlled Mechanical Buckling for Origami-Inspired Construction of 3D Microstructures in Advanced Materials," *Advanced Functional Materials*, vol. 26, no. 16, pp. 2629–2639, 2016.

[75] J. H. Jang, C. Y. Koh, K. Bertoldi, M. C. Boyce, and E. L. Thomas, "Combining Pattern Instability and Shape-Memory Hysteresis for Phononic Switching," *Nano Letters*, vol. 9, no. 5, pp. 2113–2119, 2009.